

# Computing Minimal Surfaces with Differential Forms

STEPHANIE WANG and ALBERT CHERN, University of California, San Diego, USA

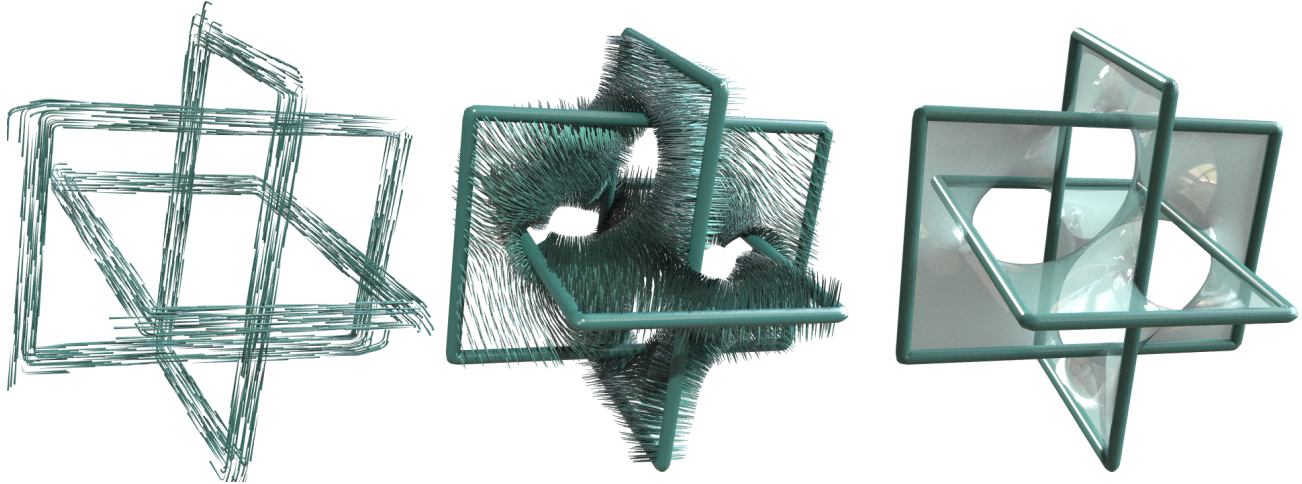


Fig. 1. Computing the minimal surface subject to Borromean rings boundary: first, represent the boundary curve by its tangent vector field (left); next, perform minimization on the normal vector field of the target surface (middle); the resulting minimal surface (right) is guaranteed to be the global minimum and not suffer from topological issues.

We describe a new algorithm that solves a classical geometric problem: Find a surface of minimal area bordered by an arbitrarily prescribed boundary curve. Existing numerical methods face challenges due to the non-convexity of the problem. Using a representation of curves and surfaces via differential forms on the ambient space, we reformulate this problem as a convex optimization. This change of variables overcomes many difficulties in previous numerical attempts and allows us to find the global minimum across all possible surface topologies. The new algorithm is based on differential forms on the ambient space and does not require handling meshes. We adopt the Alternating Direction Method of Multiplier (ADMM) to find global minimal surfaces. The resulting algorithm is simple and efficient: it boils down to an alternation between a Fast Fourier Transform (FFT) and a pointwise shrinkage operation. We also show other applications of our solver in geometry processing such as surface reconstruction.

CCS Concepts: • **Computing methodologies** → **Physical simulation; Shape modeling**; • **Mathematics of computing** → **Partial differential equations; Numerical analysis; Geometric topology**.

Additional Key Words and Phrases: Beckmann problem, minimal surface

## ACM Reference Format:

Stephanie Wang and Albert Chern. 2021. Computing Minimal Surfaces with Differential Forms. *ACM Trans. Graph.* 40, 4, Article 247 (August 2021), 14 pages. <https://doi.org/10.1145/3450626.3459781>

Authors' address: Stephanie Wang; Albert Chern, University of California, San Diego, 9500 Gilman Dr, MC 0404, La Jolla, CA, 92093, USA.

Permission to make digital or hard copies of part or all of this work for personal or classroom use is granted without fee provided that copies are not made or distributed for profit or commercial advantage and that copies bear this notice and the full citation on the first page. Copyrights for third-party components of this work must be honored. For all other uses, contact the owner/author(s).

© 2021 Copyright held by the owner/author(s).

0730-0301/2021/8-ART247

<https://doi.org/10.1145/3450626.3459781>

## 1 INTRODUCTION

A classical challenge in computational differential geometry is the Plateau problem [Lagrange 1762, pp. 354]:

*Extend a given boundary space curve into a surface with minimal area.*

The resulting *minimal surfaces* provide one of the most iconic classes of surfaces presented in mathematical visualizations [Hoffman and Matisse 1987; Weber 2013; Arnez et al. 2007]. Minimal surfaces model the physical shapes of soap films at equilibrium under surface tension [Plateau 1873; Isenberg 1978], and, inspired by this equilibrium principle, such surfaces are also the basis for modeling many microscopic structures in nature [Kirkensgaard et al. 2014; Evans and Schröder-Turk 2015] as well as for many aesthetic designs in architectures [Emmer 2013].

One of the main challenges in the computational Plateau problem is that the minimization problem is apparently non-convex. There are many examples in which a boundary curve admits multiple local minima of the area functional. These multiple minimal surfaces of



Fig. 2. Two local minima of the Plateau problem subject to the same boundary curve.

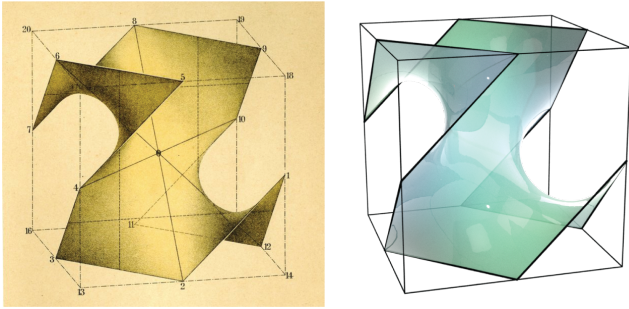


Fig. 3. Classical Schwarz minimal surface subject to a Z-shaped boundary [Schwarz 1890, Tafel 2].

the same boundary may have the same or different topologies. In fact, many topological types of surfaces do not admit any minimal surface for a given boundary curve. A numerical area-minimization algorithm can diverge if the initial guess of the surface has the wrong topology. An example in Figure 4 shows how a wrong initial configuration could lead to unstable computations.

To overcome these difficulties, we take one step back and reexamine the subject of surface representations. We ask how we can parameterize our optimization domain—the space of surfaces—so that all surfaces, even those of different topological types, can be searched within one connected set. The common explicit surface representations, such as the ones using parametric surfaces or discrete meshes, lead to disconnected search spaces across different surface topologies. The other common paradigm is the implicit level-set surface representation, which is robust under topological changes. However, the standard level-sets can only describe watertight closed surfaces, whereas the surfaces in the Plateau problem have prescribed boundaries.

We use an often-overlooked representation of curves and surfaces based on *geometric measure theory*. In this representation, each curve or surface is depicted by a *differential form* on the ambient space. Similar to the implicit level-set representation, the differential form representation is immune to topological changes of surfaces. Additionally, curves and surfaces represented by differential forms

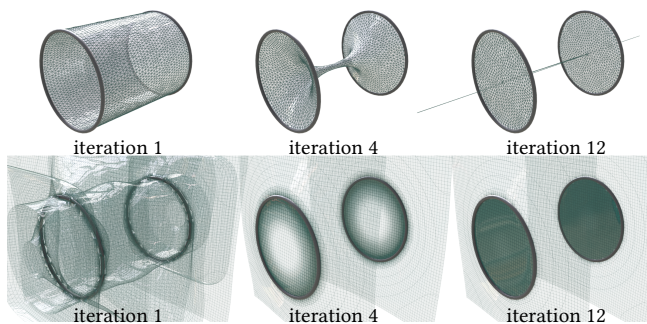


Fig. 4. Top: Using mesh-based minimal surface solvers, a wrong initial mesh could lead to a degenerate configuration, causing unstable computations and requiring topological changes. Bottom: Our geometric measure theoretic approach resolves the minimal surface regardless of its homotopy class.



Fig. 5. Left: a tetrahedroid (Jorge–Meeks 4-noid) is a minimal surface with the symmetry of a regular tetrahedron and boundary curve of four symmetrically positioned circles. Right: a squared Enneper surface with four pedals.

are allowed to have boundaries, as opposed to those represented by the level-sets of functions. The most powerful aspect of the differential form representation is that the seemingly non-convex Plateau problem becomes a *convex* optimization problem. This convex optimization problem is reminiscent to a *Beckmann optimal transport problem* [Santambrogio 2015; Solomon et al. 2014].

Using the differential form representation, we describe a straightforward algorithm to find the globally minimal surface for any given boundary curve. Our new algorithm is efficient: it only involves alternating between the fast Fourier transform (FFT) and parallelizable local operations in the ambient volume. We demonstrate using our algorithm to find the minimal surfaces for various boundary curves. In addition, we show that our minimal surface solver has an application in surface reconstruction.

### 1.1 Related Work

There has been a long history of research in computational minimal surfaces. A common approach in mathematical visualizations is to evaluate explicit solutions using the *Weierstrass–Enneper parameterization* [Hoffman and Matisse 1987; Weber 2013; Karcher and Polthier 1996]. This parameterization is a formula which always produces surfaces with vanishing mean curvature (*i.e.* minimal surfaces) via a pair of complex analytic functions. Discrete analogues of Weierstrass–Enneper’s complex analytical theory are also developed via discrete circle patterns [Bobenko et al. 2006] and discrete integrable systems [Bobenko and Pinkall 1994; Lam 2018; Sechelmann and Bobenko 2007]. However, a general method to control the boundary of the Weierstrass–Enneper surface to meet a prescribed boundary curve has not been described. Therefore, the Weierstrass–Enneper approach has not yet been applicable to the Plateau problem.

The majority of numerical approaches to the Plateau problem rely on discretizing the surface into a mesh. Douglas [1927] pioneered a multigrid finite difference method to solve the minimal surface equation when the surface is parameterized as a height field. This function graph parametric equation was also solved via a Newton-like root finding algorithm under a finite difference [Concus 1967] and a finite element [Hinata et al. 1974] discretization. Wilson [1961] explored a discrete conformal parameterization reducing the minimal surface equation into a harmonicity condition. Beyond parametric methods, Wagner [1977] minimized the area functional for general

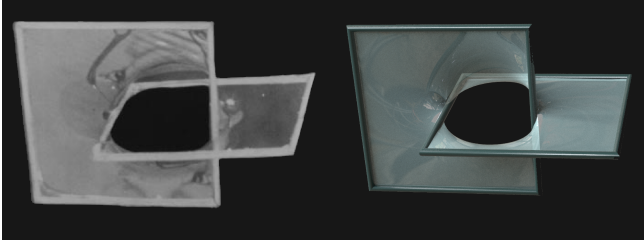


Fig. 6. Our minimal surface solver computes a result (right) comparable to a real soap film (left) formed from two interlinked squares. Photo by Prof. Harold Parks [Parks and Pitts 1997].

unstructured triangle meshes. Wagner also demonstrated that the minimization iteration can diverge if the initial mesh has the wrong topology. The modern mesh-based Plateau problem solvers use either an  $L^2$  gradient flow of the area functional called the *mean curvature flow* [Dziuk 1990; Brakke 1992; Desbrun et al. 1999], the *stretched grid methods* [Popov 1996], the  $H^1$  Sobolev gradient flow of the area functional [Pinkall and Polthier 1993; Schumacher and Wardetzky 2019], or the projected (and Sobolev) mean curvature flows that only deform the surface conformally [Crane et al. 2011; Kazhdan et al. 2012].

Our method is aligned with the *geometric measure theory* [Federer and Fleming 1960; Morgan 2016], which is a framework that has led to a major breakthrough in the mathematical analysis of the Plateau problem since the 1960s [Fleming 2015]. In this theory, geometric shapes such as curves and surfaces are represented implicitly by fields defined on the ambient space in which the geometries are embedded. These fields are called *currents* as generalized differential forms or measures on the Grassmannian bundle. Geometric measure theory has since been discretized to perform geometric processing tasks [Mullen et al. 2007; Buet et al. 2018; Mollenhoff and Cremers 2019] and medical imaging [Charon and Trouvé 2014; Vaillant and Glaunes 2005; Glaunes et al. 2004; Durrleman et al. 2008, 2009, 2011].

The geometric measure theoretic formulation to the Plateau problem was discretized via the discrete exterior calculus [Hirani 2003] and results in the Optimal Homologous Chain Problem (OHCP) [Sullivan 1990; Dunfield and Hirani 2011; Dey et al. 2011; Cohen-Steiner et al. 2020]. In these papers, the ambient  $n$ -dimensional space is discretized into a grid or a simplicial mesh, and the Plateau problem is replaced by finding a discrete  $(n-1)$ -chain with minimal total area bordered by a prescribed closed  $(n-2)$ -chain or belonging to a prescribed homology class. The resulting minimization problem is a linear programming problem. However, the discrete area functional for these chains is not consistent with the smooth area functional of smooth surfaces. This is because the discrete chains can only be confined along the fixed directions in the given mesh, resulting in effective “Manhattan distances” rather than the Euclidean ones. This problem is less pronounced on sufficiently unstructured simplicial meshes [Dunfield and Hirani 2011] or on the cell complexes obtained by intersecting grids of sufficiently many orientations [Sullivan 1990; Parks and Pitts 2020].

Our method is closely related to another equivalent geometric measure theoretic formulation where one represents the surface as a

level set function. In particular, the minimal surface may be achieved by minimizing the *total variation* of an  $\mathbb{S}^1$ -valued function [Brezis and Mironescu 2019]. In this formulation, the boundary curve for the Plateau problem is set as the *branched curve* for the  $\mathbb{S}^1$ -valued function. This level set method was first implemented by Parks [1977; 1992] using a traditional  $\mathbb{R}$ -valued level set function. However, in this  $\mathbb{R}$ -valued level set method, the boundary for the Plateau problem can only be prescribed on the surface of a convex volume. This limitation was later overcome by the introduction of a *branch cut* surface [Parks and Pitts 1997] applied with a jump condition, which effectively emulates an  $\mathbb{S}^1$ -valued level set function. In our formulation, the Parks–Pitts branch cut is replaced by a general 1-form and the optimization steps are simplified to fast Fourier transforms.

## 2 METHOD

The primary geometric objects involved in the Plateau problem are curves and surfaces in 3D. The distinguishing feature of our approach is representing curves and surfaces as Dirac- $\delta$  forms defined over the 3D ambient space. This geometric representation translates the traditionally nonconvex optimization problem into a convex one and allows us to use convex optimization methods with guarantees for the global minimum.

Let  $M$  denote a 3-dimensional compact ambient space. Although the entire formulation works for any general compact Riemannian manifold, we assume  $M$  to be a bounded subset  $M \subseteq \mathbb{R}^3$  with the Euclidean metric.

**Problem 1** (Plateau’s problem). *Given a closed curve  $\Gamma \hookrightarrow M$ , find the oriented surface  $\Sigma \hookrightarrow M$  bordered by  $\Gamma$  with the minimal area. That is,*

$$\underset{\Sigma: \partial\Sigma=\Gamma}{\text{minimize}} \text{Area}(\Sigma). \quad (1)$$

We follow by analyzing the three components of this optimization problem: the variable, the objective function, and the constraint. First, we propose a curve/surface representation by combining distribution theory and differential forms in Section 2.1. Using this representation, the objective function  $\text{Area}(\Sigma)$  becomes the mass norm (Section 2.2), and the boundary constraint  $\partial\Sigma = \Gamma$  becomes a (linear) derivative condition (Section 2.3). Finally, we formulate the relaxation using differential forms and convexify the original problem in Section 2.5. In Section 2.6, we discuss an additional constraint required for computations on periodic domains.

### 2.1 Dirac- $\delta$ curve/surface representation

Let  $x_1, x_2, x_3$  be the Cartesian coordinates of  $M \subseteq \mathbb{R}^3$  and  $\mathbf{e}_1, \mathbf{e}_2, \mathbf{e}_3$  be the corresponding basis vectors. We associate every  $k$ -dimensional submanifold  $\Sigma \hookrightarrow M$  with an  $(3-k)$ -form  $\delta_\Sigma \in \Omega^{3-k}(M)$  with the following properties:

- $\delta_\Sigma$  has infinite magnitude at  $\Sigma$  and 0 everywhere else.
- For any  $k$ -form  $\alpha \in \Omega^k(M)$ ,  $\int_M \alpha \wedge \delta_\Sigma = \int_\Sigma \alpha$ .

We call  $\delta_\Sigma$  the *Dirac- $\delta$  form associated with submanifold  $\Sigma$* . For instance, a Dirac- $\delta$  measure  $\delta_p \in \Omega^n(M)$  is a Dirac- $\delta$   $n$ -form concentrating at a point  $p \in M$ . In [Federer and Fleming 1960], these Dirac- $\delta$  forms are referred to as *integral chains*, which form a subclass of the general *current* space.



Fig. 7. Top row: a surface  $\Sigma \hookrightarrow M$  (left) and the vector field associated with  $\mathbf{v}_\Sigma^\epsilon \in \Omega^1(M)$  (right) on a regular grid ( $\epsilon = \text{grid resolution}$ ). Bottom row: a curve  $\Gamma \hookrightarrow M$  (left) and the vector field associated with  $\mathbf{v}_\Gamma^\epsilon \in \Omega^2(M)$  (right).

One way to understand the Dirac- $\delta$  measure  $\delta_p \in \Omega^3(M)$  is to view it as the limit of  $\delta_p^\epsilon(\mathbf{x}) = \begin{cases} \frac{1}{\epsilon^3 4\pi/3}, & \text{dist}(\mathbf{x}, p) \leq \epsilon \\ 0, & \text{otherwise} \end{cases}$  as  $\epsilon \rightarrow 0$ .

Similarly, a Dirac- $\delta$  form for a  $k$ -dimensional submanifold  $\Sigma \hookrightarrow M$  is the limit of the directed impulses that are concentrated in an  $\epsilon$ -neighborhood of  $\Sigma$  with magnitude  $\mathcal{O}(\frac{1}{\epsilon^{3-k}})$ . To gain intuition, one can visualize 1-forms and 2-forms in 3D using musical isomorphisms. An 1-form  $\eta = f_1 dx_1 + f_2 dx_2 + f_3 dx_3$  is associated with a vector field  $\eta^\sharp = f_1 \mathbf{e}_1 + f_2 \mathbf{e}_2 + f_3 \mathbf{e}_3$  and a 2-form  $\omega = g_1 dx_2 \wedge dx_3 + g_2 dx_3 \wedge dx_1 + g_3 dx_1 \wedge dx_2$  with  $(\star\omega)^\sharp = g_1 \mathbf{e}_1 + g_2 \mathbf{e}_2 + g_3 \mathbf{e}_3$  [Berger 2012, pp. 732]. Here,  $\star : \Omega^k(M) \rightarrow \Omega^{3-k}(M)$  denotes the Hodge star induced by the Euclidean metric on  $M$  [Flanders 1963; Dray 1999]. The Dirac- $\delta$  form  $\delta_\Gamma$  of a curve  $\Gamma \hookrightarrow M$  ( $k = 1$ ) is then associated with the limit of a sequence of vector fields  $\mathbf{v}_\Gamma^\epsilon$  with localized singularity,

$$\mathbf{v}_\Gamma^\epsilon(\mathbf{x}) = \begin{cases} \frac{1}{\epsilon^2 \pi} \mathbf{T}_\Gamma(\text{CLOSESTPOINT}(\mathbf{x}, \Gamma)), & \text{dist}(\mathbf{x}, \Gamma) \leq \epsilon \\ \mathbf{0}, & \text{otherwise.} \end{cases} \quad (2)$$

Here,  $\mathbf{T}_\Gamma$  is the unit tangent vector of the curve  $\Gamma$ . For any arbitrary 1-form  $\eta \in \Omega^1(M)$  and its associated vector field  $\mathbf{u} = \eta^\sharp : M \rightarrow \mathbb{R}^n$ , the integral  $\int_M \mathbf{u} \cdot \mathbf{v}_\Gamma^\epsilon dV$  converges to the line integral on  $\Gamma$ ,  $\int_\Gamma \mathbf{u} \cdot \mathbf{T}_\Gamma ds = \int_\Gamma \eta$ , as  $\epsilon \rightarrow 0$ . An illustration of the vector field  $\mathbf{v}_\Gamma^\epsilon$  alongside the curve  $\Gamma$  is included in Figure 7.

In a similar fashion, the Dirac- $\delta$  form  $\delta_\Sigma$  of a surface  $\Sigma \hookrightarrow M$  ( $k = 2$ ) is associated with the limit of a sequence of vector fields  $\mathbf{v}_\Sigma^\epsilon$  with localized singularity,

$$\mathbf{v}_\Sigma^\epsilon(\mathbf{x}) = \begin{cases} \frac{1}{2\epsilon} \mathbf{N}_\Sigma(\text{CLOSESTPOINT}(\mathbf{x}, \Sigma)), & \text{dist}(\mathbf{x}, \Sigma) \leq \epsilon \\ \mathbf{0}, & \text{otherwise.} \end{cases} \quad (3)$$

In this case,  $\mathbf{N}_\Sigma$  is the unit normal vector of the surface  $\Sigma$ . For any arbitrary 2-form  $\omega \in \Omega^2(M)$  with its associated vector field  $\mathbf{w} = (\star\omega)^\sharp : M \rightarrow \mathbb{R}^n$ , the integral  $\int_M \mathbf{w} \cdot \mathbf{v}_\Sigma^\epsilon dV$  converges to the flux  $\int_\Sigma \mathbf{w} \cdot \mathbf{N}_\Sigma dS = \int_\Sigma \omega$  as  $\epsilon \rightarrow 0$ . An illustration of the vector field  $\mathbf{v}_\Sigma^\epsilon$  alongside the surface  $\Sigma$  is also included in Figure 7. Under this representation, a linear combination of Dirac- $\delta$  forms  $\int_M \omega \wedge (\alpha_1 \delta_{\Sigma_1} + \alpha_2 \delta_{\Sigma_2}) = \alpha_1 \int_{\Sigma_1} \omega + \alpha_2 \int_{\Sigma_2} \omega$  describes a weighted superposition of submanifolds. In Section 2.5, we use this arithmetic

of submanifold superposition as the key to convexify the geometric optimization of surfaces.

## 2.2 Mass norm on Dirac- $\delta$ forms

We are interested in measuring the surface area of 2-dimensional submanifolds  $\Sigma \hookrightarrow M$  for Problem 1. This surface area equals the maximal flux of the bounded-length vector fields:

$$\text{Area}(\Sigma) = \int_\Sigma 1 dS = \sup_{\mathbf{v}: M \rightarrow \mathbb{R}^3, |\mathbf{v}| \leq 1} \int_\Sigma \mathbf{v} \cdot \mathbf{N}_\Sigma dS. \quad (4)$$

We now rewrite this area formula in terms of the Dirac- $\delta$  form  $\delta_\Sigma$  by linking vector fields and 2-forms. Using the Hodge star and musical isomorphisms, each vector field  $\mathbf{v}$  is uniquely associated with a 2-form  $\omega$  such that  $\mathbf{v} = (\star\omega)^\sharp$ . The pointwise Euclidean norm  $|\mathbf{v}(p)|$  has the same value as  $\sqrt{\star(\omega \wedge \star\omega)}_p$  for each  $p \in M$ . As a result, the maximal length of  $\mathbf{v}$  is the same as the max norm of  $\omega$ :

$$\|\omega\|_{\max} = \max_{p \in M} \sqrt{\star(\omega \wedge \star\omega)}_p = \max_{p \in M} |\mathbf{v}(p)|. \quad (5)$$

The supremum in (4) is taken over all bounded-length vector fields. Equivalently, we can take the supremum over the max norm unit ball in  $\Omega^2(M)$ ,

$$\text{Area}(\Sigma) = \sup_{\omega \in \Omega^2(M), \|\omega\|_{\max} \leq 1} \int_M \omega \wedge \delta_\Sigma = \|\delta_\Sigma\|_{\text{mass}}, \quad (6)$$

where

$$\|\eta\|_{\text{mass}} = \sup_{\omega \in \Omega^2(M), \|\omega\|_{\max} \leq 1} \int_M \omega \wedge \eta \quad (7)$$

is the mass norm of  $\eta \in \Omega^1(M)$ , also understood as the dual of the max norm  $\|\cdot\|_{\max}$ . The mass norm is also used in a few recent papers to convexify problems while encouraging sparsity e.g. [Soliman et al. 2018].

## 2.3 Boundary operator and exterior derivatives

We rephrase the boundary cure constraint  $\partial\Sigma = \Gamma$  into a differential constraint on Dirac- $\delta$  forms. Take an arbitrary 1-form  $\eta \in \Omega^1(M)$  that vanishes on boundary  $\partial M$ ,

$$\begin{aligned} \int_M \eta \wedge \delta_{\partial\Sigma} &= \int_{\partial\Sigma} \eta \stackrel{\text{Stokes}'}{=} \int_\Sigma d\eta = \int_M d\eta \wedge \delta_\Sigma \\ &= \oint_{\partial M} \eta \wedge \delta_\Sigma + \int_M \eta \wedge d\delta_\Sigma = \int_M \eta \wedge d\delta_\Sigma. \end{aligned} \quad (8)$$

Since  $\eta \in \Omega_0^1(M)$  is arbitrary, the above equations show that  $\delta_{\partial\Sigma} = d\delta_\Sigma$ . This link between the boundary operator  $\partial$  and the exterior derivative  $d$  leads to the following fact:

$$\partial\Sigma = \Gamma \iff d\delta_\Sigma = \delta_\Gamma. \quad (9)$$

As a result, we can replace the boundary cure constraint  $\partial\Sigma = \Gamma$  in Problem 1 with a differential (thus linear) constraint  $d\delta_\Sigma = \delta_\Gamma$ .

## 2.4 Exterior anti-derivatives

In subsequent sections (Section 3.3 and Section 4.1), we encounter the problem of solving  $d\eta = \omega$  given  $\omega \in \Omega^k(M)$  in the least-squares sense. To uniquely define a pseudo-inverse  $d^+$  of the exterior derivative  $d$ , we first project  $\omega$  onto the space of all exact forms

$\tilde{\omega} = \mathcal{P}_{\text{im}(d^{k-1})}(\omega)$  and take the solution with minimal magnitude to the feasible equation  $d\eta = \tilde{\omega}$ .

$$\begin{aligned} \tilde{\omega} &= \underset{\tilde{\omega} \in \text{im } d}{\text{argmin}} \|\tilde{\omega} - \omega\|_{L^2} \\ d^+ \omega &= \underset{d\eta = \tilde{\omega}}{\text{argmin}} \|\eta\|_{L^2}. \end{aligned} \quad (10)$$

We proceed to discuss the linear equations that arise from the above projection problem in different dimensions. These equations are also thoroughly discussed in [Zhao et al. 2019].

**2.4.1 Biot–Savart field for 2-forms.** Finding a 1-form  $\eta$  satisfying  $d\eta = \omega$  is a well-known subroutine in vorticity-streamfunction fluid simulation, e.g. [Elcott et al. 2007, Appendix B]. In that context, the 2-form  $\omega$  is the vorticity field and the resulting 1-form  $\eta = d^+ \omega$  is the corresponding divergence-free (coexact) velocity field. Using the Hodge star  $\star : \Omega^k(M) \rightarrow \Omega^{3-k}(M)$  induced from the metric, the Euler-Lagrange equation of (10) on 2-form  $\omega \in \Omega^2(M)$  is a Poisson equation on an auxiliary 2-form  $\psi \in \Omega^2(M)$ :

$$(d \star d \star - \star d \star d) \psi = \omega \quad (11)$$

$$d^+ \omega = \star d \star \psi. \quad (12)$$

The name *Biot–Savart* comes from electromagnetism, where the 2-form  $\omega = \delta_\Gamma$  represents the electric current on a circuit  $\Gamma$ , and  $\eta = d^+ \delta_\Gamma$  is the magnetic field induced by the electric current. In Section 3.3, we apply this particular operation on Dirac- $\delta$  2-form  $\delta_\Gamma$  to find the initial guess of our optimization process.

**2.4.2 Pressure solve for 1-forms.** Another common appearance of the pseudo-inverse  $d^+$  is also in fluid simulation. To ensure the incompressibility of the fluid, one often takes the velocity 1-form  $\omega \in \Omega^1(M)$ , compute the scalar function  $u = d^+ \omega \in \Omega^0(M)$ , and replace the velocity with its divergence-free component  $\tilde{\omega} = \omega - du$ . This scalar function  $u = d^+ \omega \in \Omega^0(M)$  is the zero-mean solution to a Poisson equation:

$$\Delta u = - \star d \star \omega, \quad \int_M u = 0. \quad (13)$$

Since the Poisson equation is always solved up to a constant, the zero-mean solution is easily obtained by subtracting the average of any solution. In Section 4.1, we use this procedure to compute a scalar function corresponding to our optimal solution  $\delta_\Sigma$  to convert the Dirac- $\delta$  1-form to a level set.

These references to fluid dynamics are meant to help understand  $d^+$ , though this paper is not concerned with computations of fluid dynamics.

## 2.5 Optimization problem

We now rewrite Problem 1 using Dirac- $\delta$  forms.

**Problem 2** (Plateau problem, with Dirac- $\delta$  forms). *Given a Dirac- $\delta$  2-form  $\delta_\Gamma$ , find the Dirac- $\delta$  1-form  $\delta_\Sigma$  satisfying  $d\delta_\Sigma = \delta_\Gamma$  with the minimal mass norm. That is,*

$$\underset{\delta_\Sigma \in \Omega^1(M): d\delta_\Sigma = \delta_\Gamma}{\text{minimize}} \|\delta_\Sigma\|_{\text{mass}}. \quad (14)$$

Now, we extend the admissible set to all 1-forms, including weighted superpositions of several surfaces, and arrive at our optimization problem.

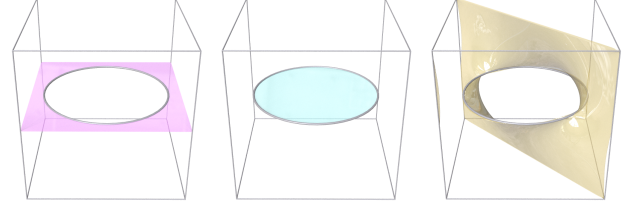


Fig. 8. The cube visualizes the periodic boundary of a box, making it a 3-dimensional torus  $\mathbb{T}^3$ . The three surfaces (pink, cyan, and yellow) are all smooth surfaces sharing the same boundary curve (circle). Without further constraints, the algorithm can converge to the pink configuration because it has the smallest surface area.

**Problem 3** (Plateau problem, all 1-forms). *Given a Dirac- $\delta$  2-form  $\delta_\Gamma$ , find the 1-form  $\eta$  satisfying  $d\delta_\Sigma = \delta_\Gamma$  with the minimal mass norm. That is,*

$$\underset{\eta \in \Omega^1(M): d\eta = \delta_\Gamma}{\text{minimize}} \|\eta\|_{\text{mass}}. \quad (15)$$

The effectiveness of the relaxation depends on the relaxed problem yielding the same minimum as the original one. Thankfully, this is a classical result from geometric measure theory [Federer and Fleming 1960, Corollary 9.6].

## 2.6 Periodic boundary condition

To speed up the computation using Fast Fourier Transform (FFT), we choose  $M = [0, 1) \times [0, 1) \times [0, 1)$  with the periodic boundary condition, making it a torus  $M = \mathbb{T}^3$ . This boundary condition introduces an artifact: as shown in Figure 8, all three surfaces satisfy the same boundary constraint  $d\delta_\Sigma = \delta_\Gamma$ , though the ones passing through the periodic boundary (pink and yellow) are hardly what we envision for minimal surfaces. This artifact is due to the non-trivial cohomology  $H^1(\mathbb{T}^3)$  on the periodic domain. In Figure 8, each surface  $\Sigma$  belongs to a different *homology class* (and the corresponding Dirac- $\delta$  form in a different *cohomology class*) that is described by a set of *harmonic coordinates*,

$$A_i = \int_M \vartheta_i \wedge \star \delta_\Sigma, \quad i = 1, 2, 3. \quad (16)$$

Here,  $\{\vartheta_1, \vartheta_2, \vartheta_3\} \subset H^1(\mathbb{T}^3)$  is a basis of the cohomology group.

To eliminate the degree of freedom introduced by cohomologies, we first select a basis  $\{\vartheta_1, \vartheta_2, \vartheta_3\}$  for  $H^1(\mathbb{T}^3)$  as shown in Figure 9. We then include three additional linear constraints  $\int_M \vartheta_i \wedge \star \eta = A_i$ ,  $i = 1, 2, 3$  in our minimization problem to ensure that  $\eta$  is amongst the cohomology class described by  $\vartheta_i$  and  $A_i$ ,  $i = 1, 2, 3$ . It turns out that the harmonic coordinates of a Dirac- $\delta$  form  $\delta_\Sigma$  for this basis is given by the (signed) projected area

$$\begin{aligned} A_i &= \int_M \vartheta_i \wedge \star \delta_\Sigma = \int_\Sigma \mathbf{e}_i \cdot \mathbf{N}_\Sigma dS \\ &= \int_{\mathcal{P}_{\mathbf{e}_i}(\Sigma)} |\mathbf{e}_i|^2 dS = \text{Area}(\mathcal{P}_{\mathbf{e}_i}(\Sigma)), \quad i = 1, 2, 3. \end{aligned} \quad (17)$$

The three scalars  $A_1, A_2, A_3$  form the area vector  $\mathbf{A} = (A_1, A_2, A_3) = \int_\Sigma \mathbf{N}_\Sigma dS$ , where each component  $A_i$  is equal to the signed area of the projected surface  $\mathcal{P}_{\mathbf{e}_i}(\Sigma)$  along direction  $\mathbf{e}_i$ . Fortunately, if  $\Sigma$  is a surface that doesn't pass through the periodic boundary, then the

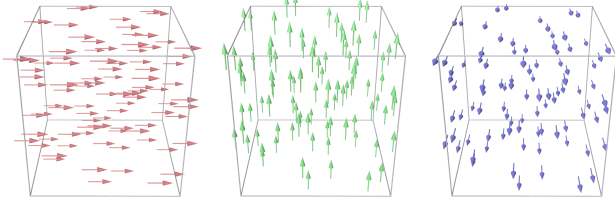


Fig. 9. We pick  $\vartheta_i = dx_i$  to be the constant vector field along the  $x$ -direction (pink),  $y$ -direction (green), and  $z$ -direction (purple). They constitute a basis of  $H^1(\mathbb{T}^3)$  such that the harmonic coordinates correspond to the (signed) projected area.

area vector  $\mathbf{A}$  can be precomputed using only the information from the boundary curve  $\Gamma = \{\mathbf{y}(t) : t \in [0, 1]\}$ :

$$\mathbf{A} = \int_{\Sigma} \mathbf{N}_{\Sigma} dS = \frac{1}{2} \oint \mathbf{y} \times d\mathbf{y}. \quad (18)$$

We show in Appendix B that the additional constraints  $\int_M \vartheta_i \wedge \star \eta = A_i$  eliminate the multiple configurations in Figure 8 down to exactly the ones that can be embedded in  $\mathbb{R}^3$  rather than just in  $\mathbb{T}^3$ . This allows us to emulate the Plateau problem in  $\mathbb{R}^3$  even if the computational domain is  $\mathbb{T}^3$ .

**Problem 4** (Plateau problem, periodic domain). *Given a Dirac- $\delta$  2-form  $\delta_{\Gamma}$  and a set of harmonic coordinates  $A_1, A_2, A_3 \in \mathbb{R}$ , find the 1-form  $\eta$  within the cohomology class that satisfies  $d\eta = \delta_{\Gamma}$  and has the minimal mass norm. That is,*

$$\text{minimize}_{\eta \in \Omega^1(M) : d\eta = \delta_{\Gamma}, \int_M \vartheta_i \wedge \star \eta = A_i} \|\eta\|_{\text{mass}}. \quad (19)$$

The *Helmholtz–Hodge decomposition* [Schwarz 2006] shows that the space of 1-forms factorizes into coexact, harmonic, and exact parts:

$$\Omega^1(M) = \ker(d^1)^{\perp} \oplus H^1(M) \oplus \text{im}(d^0). \quad (20)$$

The superscript on  $d$  indicates the degree of the differential forms; more precisely,  $\text{im}(d^0) = d(\Omega^0(M))$ ,  $\ker(d^1) = \Omega^1(M) \cap \ker(d)$ . In Problem 4, the constraints  $d\eta = \delta_{\Gamma}$  and  $\int_M \vartheta_i \wedge \star \eta = A_i$  each reduce the degree of freedom in  $\ker(d^1)^{\perp}$  and  $H^1(M)$ , leaving only flexibility

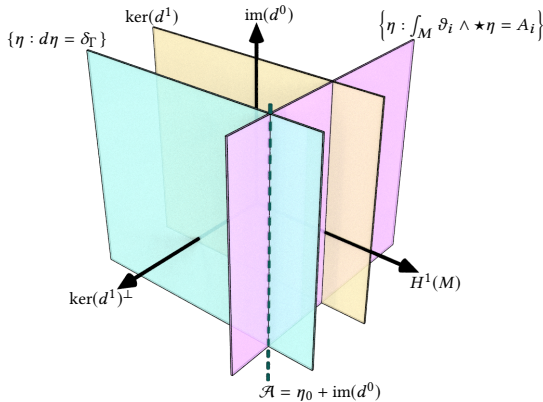


Fig. 10. Decomposing the space of all 1-forms into three components:  $\ker(d^1)^{\perp}$ ,  $H^1(M)$ , and  $\text{im}(d^0)$ . The boundary constraint  $d\eta = \delta_{\Gamma}$  (cyan plane) and the cohomology constraint  $\int_M \vartheta_i \wedge \star \eta = A_i$  (pink plane) form an intersection (green dashed line) that is parallel to  $\text{im}(d^0)$ .

in  $\text{im}(d^0)$ . We deduce that the admissible set  $\mathcal{A} = \{\eta \in \Omega^1(M) : d\eta = \delta_{\Gamma}, \int_M \vartheta_i \wedge \star \eta = A_i\} = \eta_0 + \text{im}(d^0)$  boils down to any feasible  $\eta_0 \in \mathcal{A}$  added with any exact form (Figure 10). This technique of transforming the admissible set using the Helmholtz–Hodge decomposition is also found in [Solomon et al. 2014].

**Problem 5** (Plateau problem, periodic domain (revised)). *Given an initial guess  $\eta_0 \in \Omega^1(M)$  satisfying  $d\eta_0 = \delta_{\Gamma}$  and  $\int_M \vartheta_i \wedge \star \eta_0 = A_i$ , solve*

$$\text{minimize}_{\eta \in \eta_0 + \text{im}(d^0)} \|\eta\|_{\text{mass}}. \quad (21)$$

The variability in  $\text{im}(d^0)$  can be written as a free variable  $\varphi \in \Omega^0(M)$  and  $\eta = \eta_0 + d\varphi$ :

**Problem 6** (Plateau problem, periodic domain (re-revised)). *Given an initial guess  $\eta_0 \in \Omega^1(M)$  satisfying  $d\eta_0 = \delta_{\Gamma}$  and  $\int_M \vartheta_i \wedge \star \eta_0 = A_i$ , solve*

$$\text{minimize}_{\varphi \in \Omega^0(M)} \|\eta_0 + d\varphi\|_{\text{mass}}. \quad (22)$$

### 3 ALGORITHMS

We discretize the domain  $M = \mathbb{T}^3$  by a  $n_x \times n_y \times n_z$  regular grid with spacing  $h$ .<sup>1</sup> Denote the vertex set  $V$ , edge set  $E$ , face set  $F$ , and cell set  $C$ . For a 1-form  $\eta \in \Omega^1(M)$ , we consider its vector counterpart  $\mathbf{X} = \eta^{\sharp}$ ; this vector field is discretized as  $\mathbb{R}^3$  values assigned to vertices ( $\mathbf{X} \in \mathbb{R}^{V \times 3}$ ) using a symmetric averaging relation:

$$X_{v,i} = \frac{1}{2h} \int_{v-h\mathbf{e}_i}^{v+h\mathbf{e}_i} \eta, \quad i = 1, 2, 3. \quad (23)$$

Here  $\int_{v-h\mathbf{e}_i}^{v+h\mathbf{e}_i} \eta$  denotes the integration of  $\eta$  along the line segment joining the two neighboring vertices along the direction of  $\mathbf{e}_i$ . The mass norm of a 1-form  $\eta$  is then discretized as

$$\|\eta\|_{\text{mass}} \approx \|\mathbf{X}\|_{L^1} = \sum_{v \in V} h^3 |\mathbf{X}_v| = \sum_{v \in V} \sqrt{\sum_{i=1}^3 X_{v,i}^2}. \quad (24)$$

We use  $|\mathbf{X}_v|$  to distinguish the vertex-wise Euclidean norm  $|\mathbf{X}_v| = \sqrt{X_{v,1}^2 + X_{v,2}^2 + X_{v,3}^2}$  from the global  $L^1$  norm  $\|\mathbf{X}\|_{L^1} = \sum_{v \in V} h^3 |\mathbf{X}_v|$ .

We use the Alternating Direction Method of Multiplier (ADMM) with Nesterov acceleration [Goldstein et al. 2014] on a periodic domain to solve Problem 6 numerically. We first formulate the problem into one of the following kind:

$$\begin{aligned} & \text{minimize}_{u \in \mathbb{R}^{N_u}, v \in \mathbb{R}^{N_v}} H(u) + G(v) \\ & \text{subject to } Au + Bv = b. \end{aligned}$$

**Problem 7** (Plateau problem, periodic domain, ADMM). *Given a feasible initial guess  $\mathbf{X}_0 = \eta_0^{\sharp} \in \mathbb{R}^{V \times 3}$ , solve*

$$\begin{aligned} & \text{minimize}_{\varphi \in \mathbb{R}^V, \mathbf{X} \in \mathbb{R}^{V \times 3}} \|\mathbf{X}\|_{L^1} \\ & \text{subject to } D\varphi - \mathbf{X} = -\mathbf{X}_0. \end{aligned}$$

<sup>1</sup>The computations are compliant with any mesh structure and the readers can also implement the algorithm on a tetrahedral mesh.

Here,  $(D\varphi)_{v,i} = \frac{1}{2h}(\varphi_{v+he_i} - \varphi_{v-he_i})$  is the differentiation of 0-form  $\varphi \in \mathbb{R}^V$  by the midpoint rule. In ADMM, we use the  $L^2$  inner product on vertices

$$\langle \mathbf{X}, \mathbf{Y} \rangle_{L^2} = h^3 \sum_{v \in V} \sum_{i=1}^3 X_{v,i} Y_{v,i}, \quad (25)$$

and its induced norm  $\|\mathbf{X}\|_{L^2} = \sqrt{\langle \mathbf{X}, \mathbf{X} \rangle_{L^2}} = \sqrt{\sum_{v \in V} h^3 |\mathbf{X}_v|^2}$ .

The algorithm goes as follows (taken from [Goldstein et al. 2014, Algorithm 8]):

---

**Algorithm 1** Main algorithm
 

---

**Parameter:**  $\tau > 0$  (stepping size),  $\rho \in (0, 1)$  (acceleration threshold, originally denoted as  $\eta$  in [Goldstein et al. 2014])  
**Initial:**  $\mathbf{X}, \hat{\mathbf{X}} \leftarrow \mathbf{X}_0 \in \mathbb{R}^{V \times 3}$   
**Initial:**  $\hat{\lambda}, \lambda \leftarrow \lambda_0 \in \mathbb{R}^{V \times 3}$   
 1: **for**  $k = 1, 2, \dots$  **do**  
 2:   **if**  $k > 1$  **then**  
 3:      $\mathbf{X}_{\text{prev}} \leftarrow \mathbf{X}, \lambda_{\text{prev}} \leftarrow \lambda, c_{\text{prev}} \leftarrow c$   
 4:   **end if**  
 5:    $\varphi \leftarrow \operatorname{argmin}_{\varphi} \langle \hat{\lambda}, D\varphi \rangle_{L^2} + \frac{\tau}{2} \|D\varphi - \hat{\mathbf{X}} + \mathbf{X}_0\|_{L^2}^2$  ▷ Algorithm 2  
 6:    $\mathbf{X} \leftarrow \operatorname{argmin}_{\mathbf{X}} \|\mathbf{X}\|_{L^1} - \langle \hat{\lambda}, \mathbf{X} \rangle_{L^2} + \frac{\tau}{2} \|D\varphi - \mathbf{X} + \mathbf{X}_0\|_{L^2}^2$  ▷ Algorithm 4  
 7:    $\lambda \leftarrow \hat{\lambda} + \tau(D\varphi - \mathbf{X} + \mathbf{X}_0)$   
 8:    $c \leftarrow \frac{1}{\tau} \|\lambda - \hat{\lambda}\|_{L^2}^2 + \tau \|\mathbf{X} - \hat{\mathbf{X}}\|_{L^2}^2$   
 9:   **if**  $k = 1$  **then**  
 10:      $\hat{\lambda} \leftarrow \lambda, \hat{\mathbf{X}} \leftarrow \mathbf{X}, \alpha \leftarrow 1$   
 11:   **end if**  
 12:   **if**  $c < \rho c_{\text{prev}}$  **then**  
 13:      $\alpha_+ \leftarrow \frac{1 + \sqrt{1 + 4\alpha^2}}{2}$   
 14:      $\hat{\lambda} \leftarrow \lambda + \frac{\alpha - 1}{\alpha_+} (\lambda - \lambda_{\text{prev}}), \hat{\mathbf{X}} \leftarrow \mathbf{X} + \frac{\alpha - 1}{\alpha_+} (\mathbf{X} - \mathbf{X}_{\text{prev}}), \alpha \leftarrow \alpha_+$   
 15:   **else**  
 16:      $\hat{\lambda} \leftarrow \lambda, \hat{\mathbf{X}} \leftarrow \mathbf{X}, \alpha \leftarrow 1, c \leftarrow \frac{c_{\text{prev}}}{\rho}$   
 17:   **end if**  
 18: **end for**

---

We discuss the two argmin problems arising from ADMM in Section 3.1 and Section 3.2, followed by the computation of the initial feasible guess  $\mathbf{X}_0$  in Section 3.3.

### 3.1 Solving for $\varphi$

To solve the unconstrained problem for  $\varphi$ ,

$$\operatorname{minimize}_{\varphi} \langle \hat{\lambda}, D\varphi \rangle_{L^2} + \frac{\tau}{2} \|D\varphi - \hat{\mathbf{X}} + \mathbf{X}_0\|_{L^2}^2,$$

we first derive its optimality condition:

$$h^3 D^\top \hat{\lambda} + \tau h^3 D^\top (D\varphi - \hat{\mathbf{X}} + \mathbf{X}_0) = 0.$$

We intentionally chose periodic domain  $M = \mathbb{T}^3$  so we can apply Fast Fourier Transform (FFT) to solve this Poisson equation:

$$\varphi = \Delta^{-1} \left( D^\top (\hat{\mathbf{X}} - \mathbf{X}_0) - \frac{1}{\tau} D^\top \hat{\lambda} \right), \quad (26)$$

where  $\Delta = D^\top D$  is the (positive semi-definite) Laplacian operator. We summarize this process as the following subroutines:

---

**Algorithm 2** First argmin subroutine
 

---

**Input:**  $\tau > 0$   
**Input:**  $\hat{\lambda}, \mathbf{X}_0, \hat{\mathbf{X}} \in \mathbb{R}^{V \times 3}$   
 1:  $\mathbf{Y} \leftarrow \hat{\mathbf{X}} - \mathbf{X}_0 - \frac{1}{\tau} \hat{\lambda}$   
 2:  $\varphi \leftarrow D^\top \mathbf{Y}$  ▷ by Algorithm 3  
 3:  $\varphi \leftarrow \operatorname{POISSON}\operatorname{SOLVE}(\varphi)$   
**Output:**  $\varphi \in \mathbb{R}^V$

---



---

**Algorithm 3** Poisson solver by FFT on  $\mathbb{T}^3$ 


---

**Input:**  $\Phi \in \mathbb{R}^V$   
 Denote  $V = \{0, \dots, n_x - 1\} \times \{0, \dots, n_y - 1\} \times \{0, \dots, n_z - 1\}$   
 1:  $\Phi \leftarrow \operatorname{FASTFOURIERTRANSFORM}(\Phi)$   
 2: **for**  $v = (i_x, i_y, i_z) \in V$  **do**  
 3:   **if**  $v \neq (0, 0, 0)$  **then**  
 4:      $(k_x, k_y, k_z) \leftarrow 2\pi (i_x/n_x, i_y/n_y, i_z/n_z)$   
 5:      $w \leftarrow 4 \left( \sin^2(k_x/2) + \sin^2(k_y/2) + \sin^2(k_z/2) \right)$   
 6:      $\Phi_v \leftarrow \frac{1}{w} \Phi_v$   
 7:   **end if**  
 8: **end for**  
 9:  $\varphi \leftarrow \operatorname{INVERSEFASTFOURIERTRANSFORM}(\Phi)$   
**Output:**  $\varphi \in \mathbb{R}^V$  (solution to  $\Delta\varphi = \Phi$ )

---

### 3.2 Solving for $\mathbf{X}$

The unconstrained problem involving  $\mathbf{X}$ ,

$$\operatorname{minimize}_{\mathbf{X}} \sum_{v \in V} h^3 |\mathbf{X}_v| - \langle \hat{\lambda}, \mathbf{X} \rangle_{L^2} + \frac{\tau}{2} \|D\varphi - \mathbf{X} + \mathbf{X}_0\|_{L^2}^2, \quad (27)$$

is fully decomposed into pointwise local problems. For each vertex  $v \in V$ , solve

$$\operatorname{minimize}_{\mathbf{X}_v} |\mathbf{X}_v| - \langle \hat{\lambda}_v, \mathbf{X}_v \rangle + \frac{\tau}{2} |(D\varphi)_v - \mathbf{X}_v + (\mathbf{X}_0)_v|^2. \quad (28)$$

This minimization is amenable to Shrinkage mapping,

$$\mathbf{X}_v = \operatorname{SHRINK}_{\frac{1}{\tau}} \left( \tau \hat{\lambda}_v + (D\varphi)_v + (\mathbf{X}_0)_v \right), \quad (29)$$

where the Shrinkage is given by  $\operatorname{SHRINK}_{\frac{1}{\tau}}(\mathbf{z}) = \max\left(1 - \frac{1}{\tau|\mathbf{z}|}, 0\right) \mathbf{z}$ .

---

**Algorithm 4** Second argmin subroutine
 

---

**Input:**  $\tau > 0$   
**Input:**  $\hat{\lambda}, \in \mathbb{R}^{V \times 3}, \mathbf{X}_0, D\varphi \in \mathbb{R}^{V \times 3}$   
 1: **for**  $v \in V$  **do**  
 2:    $\mathbf{Z}_v \leftarrow \tau \hat{\lambda}_v + (D\varphi)_v + (\mathbf{X}_0)_v$   
 3:   **if**  $\tau |\mathbf{Z}_v| > 1$  **then**  
 4:      $\mathbf{X}_v \leftarrow \left(1 - \frac{1}{\tau |\mathbf{Z}_v|}\right) \mathbf{Z}_v$   
 5:   **else**  
 6:      $\mathbf{X}_v \leftarrow 0$   
 7:   **end if**  
 8: **end for**  
**Output:**  $\mathbf{X} \in \mathbb{R}^{V \times 3}$

---

### 3.3 Initial guess

In this section, we go through the computational aspects of transforming a boundary curve  $\Gamma \hookrightarrow M$  into a valid initial guess  $\mathbf{X}_0 = \eta_0^\# \in \mathbb{R}^{V \times 3}$  for Algorithm 1.

Following Discrete Exterior Calculus (DEC) [Hirani 2003], 1-forms are stored as values on the edge set  $\eta_e = \int_e \eta, e \in E$  and 2-forms are stored as values on the face set  $\omega_f = \int_f \omega, f \in F$ . We can take advantage of the periodic domain and identify the edge set and the face set  $E \cong F \cong V \times \{1, 2, 3\}$  in the following manner: 1-forms  $\eta \in \Omega^1(\mathbb{T}^3)$  are stored on the vertex set  $V$  with  $i = 1, 2, 3$ ,

$$\eta_{i,v} = \int_v^{v+he_i} \eta. \quad (30)$$

2-forms  $\omega \in \Omega^2(\mathbb{T}^3)$  are also stored on vertex set  $V$  for  $i = 1, 2, 3$ ,

$$\omega_{i,v} = \iint_{[v, v+he_j] \times [v, v+he_k]} \omega, \quad \text{where } \varepsilon_{ijk} = 1. \quad (31)$$

Here  $\varepsilon_{ijk}$  is the Levi-Civita symbol and the integral is taken on the face with normal  $\mathbf{e}_i$  based at vertex  $v$ .

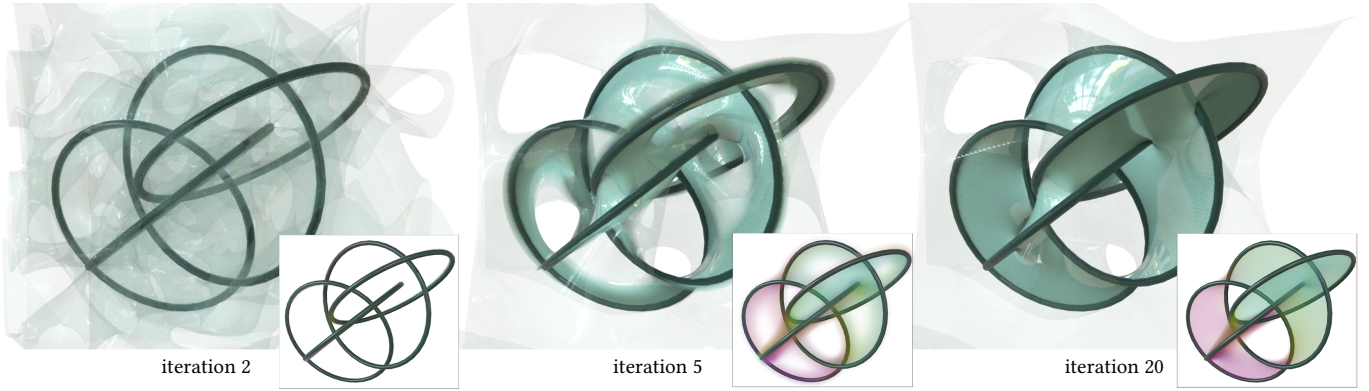


Fig. 11. Iteration sequence of the minimal surface subject to the boundary curve of four randomly positioned rings. The level set surface has an opacity proportional to the magnitude of  $\eta$ . The inserts show  $\eta$  as volumetric data with color given by the direction of  $X = \eta^\sharp$ .

The goal of this section is to seek a 1-form  $\eta_0$  that (a) satisfies  $d\eta_0 = \delta_\Gamma$  and (b) is of the desired cohomology class. We first convert the curve input  $\Gamma$  into its Dirac- $\delta$  2-form  $\delta_\Gamma \in \Omega^2(M)$ , find a 1-form  $\tilde{\eta}_0$  that satisfies  $d\tilde{\eta}_0 = \delta_\Gamma$  using Biot-Savart field, then add a harmonic 1-form  $h \in H^1(M)$  to  $\eta_0 = \tilde{\eta}_0 + h$  to ensure the projected area condition (18). The whole process is summarized in Algorithm 5.

**3.3.1 Signed intersection  $\delta_\Gamma$ .** The 2-form  $\delta_\Gamma$  associated with the curve  $\Gamma$  satisfies the following property:

$$\int_S \delta_\Gamma = \text{SIGNEDINTERSECTION}(\Gamma, S) \text{ for any surface } S \hookrightarrow M.$$

A discrete version of the 2-form  $\delta_\Gamma$  is, with  $\varepsilon_{ijk} = 1$ ,

$$(\delta_\Gamma)_{i,v} = \text{SIGNEDINTERSECTION}(\Gamma, [v, v + \mathbf{h}e_j] \times [v, v + \mathbf{h}e_k]), \quad (32)$$

**3.3.2 Biot-Savart field of  $\delta_\Gamma$ .** In Section 2.4.1, the Biot-Savart field for a 2-form  $\omega$  is given by a Poisson equation on 2-forms,

$$(d \star d \star - \star d \star d) \psi = \omega \quad (33)$$

$$\tilde{\eta}_0 = \star d \star \psi \quad (34)$$

On a regular grid, the problem decouples into three scalar Poisson equations. For each direction  $\mathbf{e}_i, i = 1, 2, 3$ , let  $F_i \subset F$  denote the collection of faces with normal  $\mathbf{e}_i$ ; since  $M = \mathbb{T}^3$  is a periodic domain, the face subset has the same structure as the vertex set  $F_i \cong V$ . Let  $\psi|_{F_i}$  (resp.  $\delta_\Gamma|_{F_i}$ ) be the restriction of  $\psi$  (resp.  $\delta_\Gamma$ ) on the subset  $F_i \cong V$ . Identifying each  $\psi|_{F_i}$  (resp.  $\delta_\Gamma|_{F_i}$ ) as a scalar function on the vertex set  $V$ , (33) is solved with three independent scalar Poisson equations:

$$\Delta \psi|_{F_i} = \delta_\Gamma|_{F_i}, \quad i = 1, 2, 3. \quad (35)$$

The discrete operation  $\Delta \psi$  for (34) is computed on each edge  $e \in E$ ,

$$(\tilde{\eta}_0)_e = \sum_{f \text{ incident to } e} s_{f,e} \psi_f. \quad (36)$$

Here  $s_{f,e} = \pm 1$  indicates whether  $e$  is positively oriented with respect to the orientation of  $f$ .

**3.3.3 Projected area adjustment.** In Section 2.6, we concluded that the initial guess  $\eta_0 \in \Omega^1(M)$  should satisfy

$$\int_M \eta_0 \wedge \star dx_i = \frac{1}{2} \mathbf{e}_i \cdot \oint \boldsymbol{\gamma} \times d\boldsymbol{\gamma}. \quad (37)$$

We compute the desired area vector  $\mathbf{A} = \frac{1}{2} \oint \boldsymbol{\gamma} \times d\boldsymbol{\gamma}$  using the input data  $\Gamma$ , compute the integral  $\int_M \tilde{\eta}_0 \wedge \star dx_i$ , and add the difference as a constant 1-form  $\vartheta$  to  $\tilde{\eta}_0$ .

---

#### Algorithm 5 Computing an initial guess

---

**Input:**  $\Gamma \hookrightarrow \mathbb{T}^3$  a discrete curve data  
Denote  $V = \{0, \dots, n_x - 1\} \times \{0, \dots, n_y - 1\} \times \{0, \dots, n_z - 1\}$   
1: **for**  $v \in V, i = 1, 2, 3$  **do**  
2:   Let  $f$  be the face perpendicular to  $\mathbf{e}_i$  based at vertex  $v$   
3:    $(\delta_\Gamma)_{i,v} = \text{SIGNEDINTERSECTION}(\Gamma, f)$   
4: **end for**  
5: **for**  $i = 1, 2, 3$  **do**  
6:    $\boldsymbol{\psi}_i \leftarrow \text{POISSONSOLVE}((\delta_\Gamma)_i)$  ▷ by Algorithm 3  
7: **end for**  
8: **for**  $v \in V, i = 1, 2, 3$  **do**  
9:   Let  $j, k \in \{1, 2, 3\}$  such that  $\varepsilon_{ijk} = 1$   
10:    $(\tilde{\eta}_0)_{i,v} \leftarrow \boldsymbol{\psi}_{j,v} - \boldsymbol{\psi}_{j,v - \mathbf{h}e_k} + \boldsymbol{\psi}_{k,v} - \boldsymbol{\psi}_{k,v - \mathbf{h}e_j}$   
11: **end for**  
12:  $\mathbf{A} \leftarrow \text{AREAVECTOR}(\Gamma)$   
13: **for**  $v \in V, i = 1, 2, 3$  **do**  
14:    $\mathbf{A} \leftarrow \mathbf{A} - (\tilde{\eta}_0)_{i,v} \mathbf{e}_i$   
15: **end for**  
16:  $\mathbf{X}_0 = \mathbf{0}$   
17: **for**  $v \in V, i = 1, 2, 3$  **do**  
18:    $(\eta_0)_{i,v} \leftarrow (\tilde{\eta}_0)_{i,v} + \mathbf{A}_i$   
19: **end for**  
20: **for**  $v \in V, i = 1, 2, 3$  **do**  
21:    $(\mathbf{X}_0)_{i,v} \leftarrow \frac{1}{2h} ((\eta_0)_{i,v} - (\eta_0)_{i,v - \mathbf{h}e_i})$   
22: **end for**  
**Output:**  $\mathbf{X}_0 \in \mathbb{R}^{V \times 3}$

---

## 4 RESULTS

All of our algorithms are implemented using Houdini FX 18.0 and run on a MacBook Pro with 8 cores and 16 GB memory. The computational bottleneck is the two FFT procedures in Algorithm 3; each FFT takes, on average 27 seconds on a  $256 \times 256 \times 256$  regular grid and the computation time is independent of the input curve  $\Gamma$ . All source code are available online in the form of Houdini files. We apply our algorithm to various boundary curves and the results are

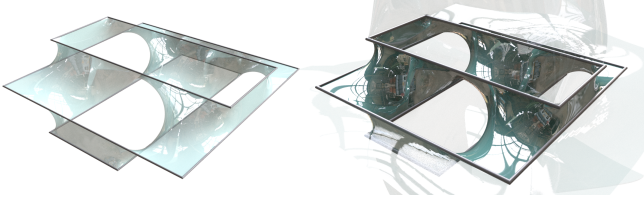


Fig. 12. Left: Costa's surface with squared frames. Right: The isosurface of  $u = d^+ \delta_\Sigma$  is rendered with opacity proportional to the magnitude of  $\delta_\Sigma$ .

rendered in Figures 1, 3, 5, 6, 11, 12, 13, and 18. The Dirac- $\delta$  surfaces are converted into level sets for rendering purposes.

#### 4.1 Converting Dirac- $\delta$ surfaces to level sets

The output  $\eta$  of Problem 6 is a Dirac- $\delta$  form  $\delta_\Sigma$  where  $\Sigma \hookrightarrow M$  is the desired minimal surface. We adopt the Poisson surface reconstruction method [Kazhdan et al. 2006] to recover the surface  $\Sigma$  from  $\delta_\Sigma$ . In this section, we reframe this surface reconstruction step in our context involving Dirac- $\delta$  forms.

The goal is to find a function  $u \in \Omega^0(M)$  that has a jump right across  $\Sigma$ . If the jump is sufficiently large, an isosurface  $S$  of  $u$  (at a value enclosed by the jump interval) will contain  $\Sigma$ . An isosurface is always boundaryless ( $\partial S = \emptyset$ ). However, since  $\delta_\Sigma$  vanishes everywhere except at  $\Sigma$ , we can clip off parts of  $S$  using the magnitude of  $\delta_\Sigma$ , and obtain the minimal surface  $\Sigma$  with boundary  $\partial\Sigma = \Gamma$ . See Figure 12.

The 1-form  $\delta_\Sigma$  is an impulse concentrated at  $\Sigma$ ; it emulates the derivative of a jump. We then search for the 0-form  $u \in \Omega^0(M)$  whose differential  $du$  best approximates  $\delta_\Sigma$  in the least-squares sense:

$$u = \operatorname{argmin}_{u \in \Omega^0(M)} \|du - \delta_\Sigma\|_{L^2}. \quad (38)$$

This is the pseudo-inverse  $u = d^+ \delta_\Sigma$  as discussed in Section 2.4.2. Up to an additive constant, the scalar function  $u$  solves the Poisson equation

$$\Delta u = -\star d\star(\delta_\Sigma). \quad (39)$$

Next, we show that  $u$  indeed has a jump of height 1 at  $\Sigma$  and is smooth everywhere else. This is equivalent to showing that  $du = \delta_\Sigma + \xi$  for some 1-form  $\xi$  smooth on  $M \setminus \partial\Sigma$ . The optimality of (38) implies that  $du$  is the exact component of  $\delta_\Sigma$  in its Helmholtz–Hodge decomposition,

$$\delta_\Sigma = du + \delta\beta + h, \quad \text{for some } \beta \in \Omega^2(M), h \in H^1(M). \quad (40)$$

Here  $\delta = \star d\star : \Omega^2(M) \rightarrow \Omega^1(M)$  is the codifferential operator. Taking  $d$  on both sides of (40) we discover that

$$d\delta_\Sigma = d\delta\beta = \delta_\Gamma. \quad (41)$$

Therefore,  $\delta\beta$  is the unique Biot–Savart field of  $\Gamma = \partial\Sigma$ , which is smooth away from the curve  $\Gamma$ . As a result,  $du = \delta_\Sigma + \xi$  where  $\xi = -\delta\beta - h$  is a smooth 1-form on  $M \setminus \Gamma$ . Thus,  $u$  has a jump at  $\Sigma$  of height 1 and is smooth everywhere else.

#### 4.2 Validation

We first formulate a notion of distance between the true solution  $\Sigma_{\text{truth}}$  and our approximated surface  $\Sigma_{\text{approx}}$  regardless of their parametrization. Since  $\Sigma_{\text{truth}}$  and  $\Sigma_{\text{approx}}$  share the same boundary  $\Gamma = \partial\Sigma_{\text{truth}} = \partial\Sigma_{\text{approx}}$ , together they enclose a volumetric region  $U$ . The (unsigned) volume of the region  $U$  entails the distance between the two surfaces  $\Sigma_{\text{truth}}$  and  $\Sigma_{\text{approx}}$ . We test our Plateau problem solver on a classical example, helicoid, and plot the relative error using the (unsigned) volume of  $U$  in Figure 13. In addition, we plot the relative error in mass norm of each main algorithm iteration with different grid resolutions in Figure 14.

#### 4.3 Applications

Our Plateau problem solver for an arbitrary curve input can be an important tool in mathematical visualizations and physical simulations of soap films, as demonstrated by the figures throughout the preceding sections. Such a tool can benefit problems that have relied on modeling minimal surfaces [Aziz et al. 2016], or those that seek a surface with an appropriate topology for given boundary skeletons [Pan et al. 2015; Li et al. 2019]. In this section, we give two more proofs-of-concept to the applications of our Plateau problem solver.

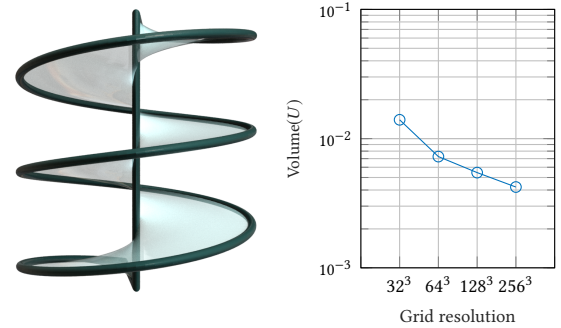


Fig. 13. Left: a classical example of minimal surfaces – helicoid. Right: the relative error in  $\text{Volume}(U)$  of the final results coming from different grid resolutions.

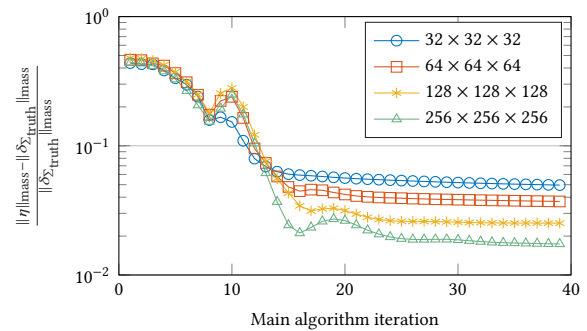


Fig. 14. The relative error in mass norm  $\frac{\|\eta\|_{\text{mass}} - \|\delta_{\Sigma_{\text{truth}}}\|_{\text{mass}}}{\|\delta_{\Sigma_{\text{truth}}}\|_{\text{mass}}}$  for each ADMM iteration. The four curves corresponds to computations on regular grids with different resolutions.

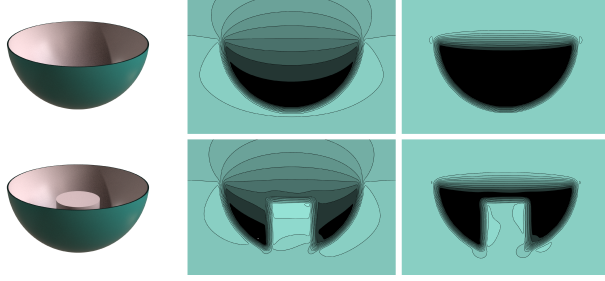


Fig. 15. To reconstruct a watertight surface from an incomplete input (left column), we compute a function  $u$  before taking its isosurface. We plot the cross sections of  $u$  computed by Poisson reconstruction (middle column) and our watertight reconstruction (right column). Top row: a hemisphere. Bottom row: a hemisphere with a bump.

**4.3.1 Surface Reconstructions.** The general surface reconstruction problem is as formulated below.

**Problem 8** (Surface reconstruction problem). *Given some (partial) measurement of positions and normals of a surface, find a watertight surface that best fits the measurement.*

The *Poisson surface reconstruction* [Kazhdan et al. 2006] as mentioned in Section 4.1 is a standard solution to this problem. Treating the measured position and normal data as an impulse on some surface  $\Sigma_0 \hookrightarrow M$ , the input is equivalent to a Dirac- $\delta$  form  $\eta_0 = \delta_{\Sigma_0} \in \Omega^1(M)$ . When the position and normal input has missing data (due to e.g. 3D scanner noise, visibility, etc.), the input surface  $\Sigma_0$  might not be a closed surface (i.e. have “holes”). The Poisson surface reconstruction solves for a function  $u = d^+ \eta_0 \in \Omega^0(M)$  that minimizes  $\|\eta_0 - du\|_{L^2}$  and subsequently exports a level set of  $u$ . Since the function  $u$  is a least-squares solution to the incomplete input  $\Sigma_0$ , it will behave rather smoothly near the “holes”, making the final level set output dependent on the choice of the level set and giving ambiguous results. In Figure 15, the middle column illustrates how the function  $u = d^+ \eta_0$  is smooth where the input  $\Sigma_0$  is incomplete.

We propose a *watertight surface reconstruction* using our Plateau problem solver:

**Problem 9** (Watertight surface reconstruction). *Given an input  $\eta_0 = \delta_{\Sigma_0}$ , find the function  $v \in \Omega^0(M)$  such that*

$$v = \operatorname{argmin}_{\varphi \in \Omega^0(M)} \|\eta_0 - d\varphi\|_{\text{mass}}. \quad (42)$$

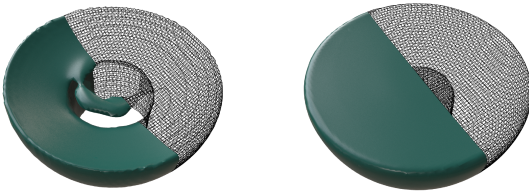


Fig. 16. For a hemisphere with a bump (bottom row of Figure 15), we use the Poisson reconstruction (left) and our watertight reconstruction (right) to complete the surface. Due to the irregular input, Poisson reconstruction yields a bumpy surface and requires tuning parameters of the isosurface, while our method yields a smooth, true watertight surface without tuning.

The only difference between (42) and the Poisson surface reconstruction is the use of mass norm instead of  $L^2$  norm. The above problem is also the same as our main optimization problem (22) except for the minus sign. Let  $v$  denote the minimizer of (42). According to previous sections,  $\eta = \eta_0 - dv$  is the Dirac- $\delta$  form corresponding to a minimal surface  $\Sigma$  that has the same boundary  $\partial\Sigma_0$  and the same homology class as the input surface  $\Sigma_0$ . The combination of the original input  $\Sigma_0$  and the minimal surface  $\Sigma$  is  $dv$ :

$$dv = \eta_0 - \eta = \delta_{\Sigma_0} - \delta_{\Sigma}. \quad (43)$$

The minimal surface  $\Sigma$  acts as the “caps” that fill the “holes” of the input  $\Sigma_0$ ; this gives us a better geometric characterization of the capping surface and thus the final isosurface output. Moreover, the resulting function  $v$  is sharp on both  $\Sigma_0$  and  $\Sigma$  ends, making the isosurface extraction unambiguous.

On a broader scope, the Poisson surface reconstruction is an example of the *Hodge decomposition*, which can be applied to differential forms of any degree. Similarly, our watertight surface reconstruction also generalizes to a new Hodge-like decomposition for forms of arbitrary degrees. This mathematical framework relates the Plateau problem to other subjects in graphics such as optimal transports. We describe this new Hodge theory in Appendix A.

**4.3.2 Curve morphing via minimal surface.** Another direct application of our Plateau problem solver is curve morphing. Our solver provides a new way of animating the interpolation between two planar closed curves. Two planar curves are placed a small distance apart to form a (closed) space curve. Using this space curve as the boundary constraint, we compute the minimal surface of which we extract the cross sections and use as interpolated curves. (See Figure 17 for configuration.) This curve morphing method guarantees minimal traversed area by the animated curve and in terms visualizes the notion of *cobordism* in topology. For more discussions on cobordism, see [Kosinski 2013, Part VII].

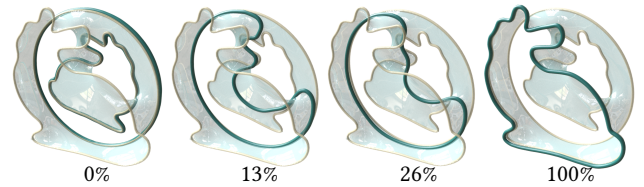


Fig. 17. Morphing an annulus into a mirrored bunny through a minimal surface. The percentages below correspond to the interpolation between annulus and bunny.

## 5 SUMMARY

This paper describes a robust numerical algorithm that solves the globally minimal surface for a given boundary curve, also as known as the Plateau problem. The computation involves only FFT and pointwise operations on a regular volumetric grid, and is guaranteed to reach the global minimum. This contrasts with the previous numerical approaches to the Plateau problem that are based on evolving surfaces using curvature flows. These previous approaches lead to local minima only if not developing singularity. The key

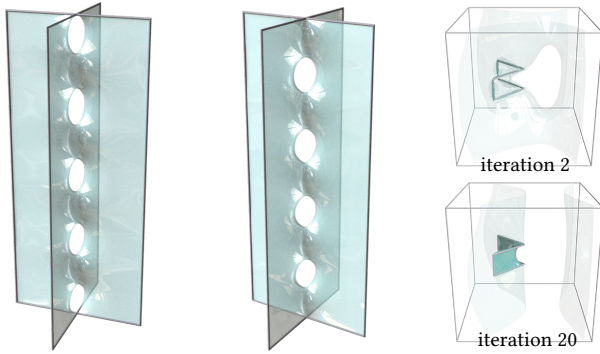


Fig. 18. Sherk's surface is a classical periodic minimal surface. Using gradient domain processing, we can quickly compute the minimization problem on a smaller boundary curve, sum over copies reflected around symmetric axis, then evaluate the level set. Left and middle: level set from 18 reflected copies of the solution. Right: the minimization process at iteration 2 and 20.

to our advancement is identifying curves and surfaces as Dirac- $\delta$  forms. Using this representation, the Plateau problem is rewritten into a convex optimization problem. This convex optimization has a straightforward generalization to differential forms of arbitrary orders, uniting the Beckmann problem in optimal transport theory and surface reconstruction problem in geometry processing. We elaborate this generalization in Appendix A.

The foundation of the Dirac- $\delta$  geometric representation is geometry measure theory. The present paper only focuses on representing orientable surfaces, which is only a special case in this larger context of geometric measure theory. For example, there are non-orientable and non-manifold surface representations involving measures on Grassmannian bundles, whose computational aspects have been drawing increasing attention [Buet et al. 2018]. We expect that these measure theoretic ways of representing geometries will bring more elegant solutions and new computational tools to previously challenging problems.

## ACKNOWLEDGMENTS

We thank Prof. Harold Parks for the soap film photograph and Benjamin Lindsay for the editorial assistance. The work was supported by Computer Science and Engineering at UCSD. Additional support was provided by SideFX software.

## REFERENCES

Andreas Arnez, Konrad Polthier, Martin Steffens, and Christian Teitzel. 2007. *Touching Soap Films (Springer VideoMATH)*. Springer-Verlag.

Moheb Sabry Aziz et al. 2016. Biomimicry as an approach for bio-inspired structure with the aid of computation. *Alexandria Engineering Journal* 55, 1 (2016), 707–714.

Marcel Berger. 2012. *A panoramic view of Riemannian geometry*. Springer Science & Business Media.

Alexander I Bobenko, Tim Hoffmann, and Boris A Springborn. 2006. Minimal surfaces from circle patterns: Geometry from combinatorics. *Annals of Mathematics* (2006), 231–264.

Alexander I Bobenko and Ulrich Pinkall. 1994. *Discrete isothermic surfaces*. Technical Report. SCAN-9412128.

Kenneth A Brakke. 1992. The surface evolver. *Experimental mathematics* 1, 2 (1992), 141–165.

Haim Brezis and Petru Mironescu. 2019. The Plateau problem from the perspective of optimal transport. *Comptes Rendus Mathématique* 357, 7 (2019), 597–612.

Blanche Buet, Gian Paolo Leonardi, and Simon Masnou. 2018. Discretization and approximation of surfaces using varifolds. *Geometric Flows* 3, 1 (2018), 28–56.

Nicolas Charon and Alain Trounev. 2014. Functional currents: a new mathematical tool to model and analyse functional shapes. *Journal of mathematical imaging and vision* 48, 3 (2014), 413–431.

David Cohen-Steiner, André Lieutier, and Julien Vuillamy. 2020. Lexicographic optimal homologous chains and applications to point cloud triangulations. In *36th International Symposium on Computational Geometry (SoCG 2020)*. Schloss Dagstuhl-Leibniz-Zentrum für Informatik.

Paul Concus. 1967. Numerical solution of the minimal surface equation. *Math. Comp.* 21, 99 (1967), 340–350.

Keenan Crane, Ulrich Pinkall, and Peter Schröder. 2011. Spin transformations of discrete surfaces. In *ACM SIGGRAPH 2011 papers*. 1–10.

Mathieu Desbrun, Mark Meyer, Peter Schröder, and Alan H Barr. 1999. Implicit fairing of irregular meshes using diffusion and curvature flow. In *Proceedings of the 26th annual conference on Computer graphics and interactive techniques*. 317–324.

Tamal K Dey, Anil N Hirani, and Bala Krishnamoorthy. 2011. Optimal homologous cycles, total unimodularity, and linear programming. *SIAM J. Comput.* 40, 4 (2011), 1026–1044.

Jesse Douglas. 1927. A method of numerical solution of the problem of Plateau. *Annals of Mathematics* (1927), 180–188.

Tevian Dray. 1999. The hodge dual operator. *Oregon State University report* (1999), 1–6.

Nathan M Dunfield and Anil N Hirani. 2011. The least spanning area of a knot and the optimal bounding chain problem. In *Proceedings of the twenty-seventh annual symposium on Computational geometry*. 135–144.

Stanley Durrleman, Pierre Fillard, Xavier Pennec, Alain Trounev, and Nicholas Ayache. 2011. Registration, atlas estimation and variability analysis of white matter fiber bundles modeled as currents. *NeuroImage* 55, 3 (2011), 1073–1090. <https://doi.org/10.1016/j.neuroimage.2010.11.056>

Stanley Durrleman, Xavier Pennec, Alain Trounev, Paul Thompson, and Nicholas Ayache. 2008. Inferring brain variability from diffeomorphic deformations of currents: an integrative approach. *Medical image analysis* 12, 5 (2008), 626–637.

Stanley Durrleman, Xavier Pennec, Alain Trounev, and Nicholas Ayache. 2009. Statistical models of sets of curves and surfaces based on currents. *Medical Image Analysis* 13, 5 (2009), 793–808. <https://doi.org/10.1016/j.media.2009.07.007> Includes Special Section on the 12th International Conference on Medical Imaging and Computer Assisted Intervention.

Gerhard Dziuk. 1990. An algorithm for evolutionary surfaces. *Numer. Math.* 58, 1 (1990), 603–611.

Sharif Elcott, Yiyang Tong, Eva Kanso, Peter Schröder, and Mathieu Desbrun. 2007. Stable, circulation-preserving, simplicial fluids. *ACM Transactions on Graphics (TOG)* 26, 1 (2007), 4–es.

Michele Emmer. 2013. Minimal surfaces and architecture: New forms. *Nexus Network Journal* 15, 2 (2013), 227.

Myfanwy E Evans and Gerd E Schröder-Turk. 2015. In a material world: Hyperbolic geometry in biological materials. *Asia Pacific Mathematics Newsletter* 5, 2 (2015), 21–30.

Herbert Federer and Wendell H Fleming. 1960. Normal and integral currents. *Annals of Mathematics* (1960), 458–520.

Harley Flanders. 1963. *Differential forms with applications to the physical sciences by harley flanders*. Elsevier.

Wendell H Fleming. 2015. Geometric measure theory at brown in the 1960s.

Joan Glaunes, Alain Trounev, and Laurent Younes. 2004. Diffeomorphic matching of distributions: A new approach for unlabelled point-sets and sub-manifolds matching. In *Proceedings of the 2004 IEEE Computer Society Conference on Computer Vision and Pattern Recognition, 2004. CVPR 2004.*, Vol. 2. IEEE, II–II.

Tom Goldstein, Brendan O'Donoghue, Simon Setzer, and Richard Baraniuk. 2014. Fast alternating direction optimization methods. *SIAM Journal on Imaging Sciences* 7, 3 (2014), 1588–1623.

Allen Hatcher. 2002. *Algebraic topology*. Cambridge University Press.

Masahiro Hinata, Masaaki Shimasaki, and Takeshi Kiyono. 1974. Numerical solution of Plateau's problem by a finite element method. *Math. Comp.* 28, 125 (1974), 45–60.

Anil Nirmal Hirani. 2003. *Discrete exterior calculus*. Ph.D. Dissertation. California Institute of Technology.

David Hoffman and Henri Matisse. 1987. The computer-aided discovery of new embedded minimal surfaces. *The Mathematical Intelligencer* 9, 3 (1987), 8–21.

Cyril Isenberg. 1978. *The science of soap films and soap bubbles*. Tieto Cleveton, UK.

Dominic Joyce. 2003. Riemannian holonomy groups and calibrated geometry. In *Calabi-Yau Manifolds and Related Geometries*. Springer, 1–68.

Hermann Karcher and Konrad Polthier. 1996. *An introduction to minimal surfaces*. <http://page.mi.fu-berlin.de/polthier/booklet/architecture.html>

Michael Kazhdan, Matthew Bolitho, and Hugues Hoppe. 2006. Poisson surface reconstruction. In *Proceedings of the fourth Eurographics symposium on Geometry processing*, Vol. 7.

Michael Kazhdan, Jake Solomon, and Mirela Ben-Chen. 2012. Can mean-curvature flow be modified to be non-singular?. In *Computer Graphics Forum*, Vol. 31. Wiley Online

- Library, 1745–1754.
- Jacob JK Kirkensgaard, Myfanwy E Evans, Liliana De Campo, and Stephen T Hyde. 2014. Hierarchical self-assembly of a striped gyroid formed by threaded chiral mesoscale networks. *Proceedings of the National Academy of Sciences* 111, 4 (2014), 1271–1276.
- Antoni A Kosinski. 2013. *Differential manifolds*. Courier Corporation.
- JL Lagrange. 1762. Essai d’une nouvelle méthode pour déterminer les maxima et les formules des intégrales minimum indéfinies. *Œuvres de Lagrange (1867–1892)* 1 (1762), 335–362.
- Wai Yeung Lam. 2018. Discrete minimal surfaces: critical points of the area functional from integrable systems. *International Mathematics Research Notices* 2018, 6 (2018), 1808–1845.
- Linhu Li, Ching Hua Lee, and Jiangbin Gong. 2019. Emergence and full 3D-imaging of nodal boundary Seifert surfaces in 4D topological matter. *Communications physics* 2, 1 (2019), 1–11.
- Thomas Mollenhoff and Daniel Cremers. 2019. Lifting vectorial variational problems: a natural formulation based on geometric measure theory and discrete exterior calculus. In *Proceedings of the IEEE Conference on Computer Vision and Pattern Recognition*. 11117–11126.
- Frank Morgan. 2016. *Geometric measure theory: a beginner’s guide*. Academic press.
- Patrick Mullen, Alexander McKenzie, Yiyong Tong, and Mathieu Desbrun. 2007. A variational approach to Eulerian geometry processing. *ACM Transactions on Graphics (TOG)* 26, 3 (2007), 66–es.
- Hao Pan, Yang Liu, Alla Sheffer, Nicholas Vining, Chang-Jian Li, and Wenping Wang. 2015. Flow aligned surfacing of curve networks. *ACM Transactions on Graphics (TOG)* 34, 4 (2015), 1–10.
- Harold Parks. 1977. Explicit determination of area minimizing hypersurfaces. *Duke Mathematical Journal* 44, 3 (1977), 519–534.
- Harold R Parks. 1992. Numerical approximation of parametric oriented area-minimizing hypersurfaces. *SIAM journal on scientific and statistical computing* 13, 2 (1992), 499–511.
- Harold R Parks and Jon T Pitts. 1997. Computing least area hypersurfaces spanning arbitrary boundaries. *SIAM Journal on Scientific Computing* 18, 3 (1997), 886–917.
- Harold R Parks and Jon T Pitts. 2020. Explicit determination in  $\mathbb{R}^N$  of  $(N - 1)$ -dimensional area minimizing surfaces with arbitrary boundaries. *The Journal of Geometric Analysis* 30, 1 (2020), 601–616.
- Ulrich Pinkall and Konrad Polthier. 1993. Computing discrete minimal surfaces and their conjugates. *Experimental mathematics* 2, 1 (1993), 15–36.
- Joseph Plateau. 1873. *Statique expérimentale et théorique des liquides soumis aux seules forces moléculaires*. Vol. 1. Gauthier-Villars.
- EV Popov. 1996. On some variational formulations for minimum surface. *Transactions of the Canadian Society for Mechanical Engineering* 20, 4 (1996), 391–400.
- Filippo Santambrogio. 2015. Optimal transport for applied mathematicians. *Birkhäuser*, NY 55, 58–63 (2015), 94.
- Henrik Schumacher and Max Wardetzky. 2019. Variational convergence of discrete minimal surfaces. *Numer. Math.* 141, 1 (2019), 173–213.
- Günter Schwarz. 2006. *Hodge Decomposition-A method for solving boundary value problems*. Springer.
- Hermann Amandus Schwarz. 1890. *Gesammelte mathematische abhandlungen*. Berlin J. Springer.
- Stefan Sechelmann and Alexander I Bobenko. 2007. *Discrete minimal surfaces, Koebe polyhedra, and Alexandrov’s theorem. variational principles, algorithms, and implementation*. Ph.D. Dissertation. Citeseer.
- Yousuf Soliman, Dejan Slepčev, and Keenan Crane. 2018. Optimal cone singularities for conformal flattening. *ACM Transactions on Graphics (TOG)* 37, 4 (2018), 1–17.
- Justin Solomon, Raif Rustamov, Leonidas Guibas, and Adrian Butscher. 2014. Earth mover’s distances on discrete surfaces. *ACM Transactions on Graphics (TOG)* 33, 4 (2014), 1–12.
- John M Sullivan. 1990. A crystalline approximation theorem for hypersurfaces. ProQuest LLC. *Ann Arbor, Thesis (Ph. D.), Princeton University* (1990).
- Marc Vaillant and Joan Glaunes. 2005. Surface matching via currents. In *Biennial International Conference on Information Processing in Medical Imaging*. Springer, 381–392.
- H-J Wagner. 1977. A contribution to the numerical approximation of minimal surfaces. *Computing* 19, 1 (1977), 35–58.
- Matthias Weber. 2013. *Minimal surface archive*. <https://minimal.sitehost.iu.edu/archive/index.html>
- Walter L Wilson. 1961. On discrete Dirichlet and Plateau problems. *Numer. Math.* 3, 1 (1961), 359–373.
- Rundong Zhao, Mathieu Desbrun, Guo-Wei Wei, and Yiyong Tong. 2019. 3D Hodge decompositions of edge-and face-based vector fields. *ACM Transactions on Graphics (TOG)* 38, 6 (2019), 1–13.

## A A NEW HODGE THEORY

Throughout the paper, we have been focusing on 2-dimensional minimal surfaces embedded in  $\mathbb{R}^3$  (or a 3-torus). In the differential form representation, we minimize the mass norm of a 1-form  $\eta$  (for the surface being codimension 1) subject to an equality constraint on  $d\eta$  and the cohomology class. In this appendix, we show that this geometric optimization is much more general than that with the specific dimension and codimension above. In this broader view, we will see that the mass norm minimization problem includes the *Beckmann optimal transport problem* as a special case. We also see that the general optimality condition for the mass minimization gives a convex yet nonlinear version for the Helmholtz–Hodge decomposition. Note that this can lead to many implications, since the classical Helmholtz–Hodge decomposition underpins many fundamental tasks in geometry processing. One of the applications of the Helmholtz–Hodge decomposition is *Poisson surface reconstruction*. As detailed in Section 4.3.1, by applying the new Hodge theory, we obtain the nonlinear counterpart to this surface reconstruction method using our minimal mass problem.

In the following discussion, we first establish the minimal mass problem in a general dimension, unifying the Plateau problem and the Beckmann optimal transport problem. Next, we characterize the optimality condition for the minimal mass problem, similar to that in optimal transport. This optimality condition allows us to develop a Hodge decomposition theory. Finally, we interpret the new Hodge theory as the *watertight-minimal decomposition* as the theoretical foundation for Section 4.3.1.

### A.1 The General Minimal Mass Problem

Let the ambient space  $M$  be an  $n$ -dimensional Riemannian manifold. The *mass norm*  $\|\eta\|_{\text{mass}}$  of a  $k$ -form  $\eta$  is given by (cf. (7))

$$\|\eta\|_{\text{mass}} := \sup_{\substack{\omega \in \Omega^{n-k}(M) \\ \|\omega\|_{\text{max}} \leq 1}} \int_M \omega \wedge \eta. \quad (44)$$

We now generalize Problem 4 to a generic mass norm minimization problem subject to a differential constraint, with or without an additional cohomology constraint.

**Problem 10** (Minimal mass problem). *Let  $\zeta \in \Omega^{k+1}(M)$  be a prescribed exact  $(k+1)$ -form with a finite mass. Find a  $k$ -form  $\eta \in \Omega^k(M)$  which solves*

$$\begin{aligned} & \text{minimize } \|\eta\|_{\text{mass}} \\ & \eta \in \Omega^k(M) \\ & \text{subject to } d\eta = \zeta. \end{aligned} \quad (45)$$

**Problem 11** (Minimal mass problem with cohomology constraints). *Let  $\zeta \in \Omega^{k+1}(M)$  be a prescribed exact  $(k+1)$ -form with a finite mass. Let  $\eta_0 \in \Omega^k(M)$  be some  $k$ -form satisfying  $d\eta_0 = \omega$  whose purpose is to indicate a particular cohomology class  $[\eta_0] \in \Omega^k(M)/\text{im}(d)$ . Find a  $k$ -form  $\eta \in \Omega^k(M)$  which solves*

$$\begin{aligned} & \text{minimize } \|\eta\|_{\text{mass}} \\ & \eta \in \Omega^k(M) \\ & \text{subject to } d\eta = \zeta, \eta \in [\eta_0]. \end{aligned} \quad (46)$$

Similar to Problem 5, the two conditions  $d\eta = \zeta$  and  $\eta \in [\eta_0]$  combined are equivalent to  $\eta - \eta_0 \in \text{im}(d)$ . Therefore Problem 11 is equivalent to the following problem by identifying  $\eta = \eta_0 + d\alpha$ :

**Problem 12** (Equivalent to Problem 11). *Given  $\eta_0 \in \Omega^k(M)$  with  $\|d\eta_0\|_{\text{mass}} < \infty$ , solve*

$$\underset{\alpha \in \Omega^{k-1}(M)}{\text{minimize}} \|\eta_0 + d\alpha\|_{\text{mass}}. \quad (47)$$

*Codimensional Plateau Problem.* Note that when  $\zeta = \delta_\Gamma$ , where  $\Gamma$  is an  $(n - k - 1)$ -dimensional submanifold of  $M$ , we recover the generalized Plateau problem. In this case, the minimal submanifold  $\Sigma$  extracted from an optimizer  $\eta = \delta_\Sigma$  has codimension  $k$ .

*Beckmann Problem.* Optimal transport problems yield natural measurements of distance between two different measures on a space. Given two measures  $\rho_1, \rho_2$  on  $M$ ,  $\int_M \rho_1 = \int_M \rho_2$ , the *Wasserstein distance* or the *earth mover's distance* between  $\rho_1$  and  $\rho_2$  is defined as the minimal cost to transport the measure  $\rho_1$  to  $\rho_2$ . If the transportation cost is proportional to the total distance of the transportation paths, the problem can be rephrased as a vector field (describing the flow of transportation) design problem. This problem is known as the *Beckmann problem*: Find a vector field with minimal  $\int_M |\mathbf{X}| dV$  subject to  $\text{div } \mathbf{X} = \rho_1 - \rho_2$  (viewing  $\rho_1$  and  $\rho_2$  as their density function). The Beckmann problem looks elegant in terms of differential forms. View the signed measure  $\rho_1 - \rho_2$  as an  $n$ -form and represent the flow  $\mathbf{X}$  by the flux form  $((n - 1)$ -form) using the musical isomorphism  $\eta = \star(\mathbf{X}^\flat)$ . Then, the Beckmann problem asks for an  $(n - 1)$ -form  $\eta$  that

$$\begin{aligned} &\underset{\eta \in \Omega^{n-1}(M)}{\text{minimize}} \|\eta\|_{\text{mass}} \\ &\text{subject to } d\eta = \rho_1 - \rho_2, \end{aligned} \quad (48)$$

which is Problem 10 with  $k = n - 1$ . If the domain has a nontrivial  $(n - 1)$ -th cohomology, Problem 11 comes with an additional cohomology constraint restricting the transport paths to a given homotopy type.

## A.2 Optimality Conditions

The optimality condition for the Beckmann problem is known as the Monge–Kantorovich system [Santambrogio 2015, Equation 4.7]. Here, we state the optimality for our minimal mass problem in a manner analogous to the Monge–Kantorovich system.

**Definition 1** (Local mass). *Let  $\eta \in \Omega^k(M)$  be a  $k$ -form with finite mass. Then  $\eta$  gives rise to a nonnegative (Borel) measure  $\mu_\eta$  on  $M$  defined by that for each open set  $A \subset M$ ,*

$$\mu_\eta(A) = \int_A \mu_\eta := \sup_{\substack{\omega \in \Omega^{n-k}(M) \\ \|\omega\|_{\text{max}} \leq 1}} \int_A \omega \wedge \eta. \quad (49)$$

Note that  $\|\eta\|_{\text{mass}} = \mu_\eta(M) = \int_M \mu_\eta$ . If  $\eta$  is smooth, then  $\mu_\eta = |\eta|\mu$  where  $\mu$  is the volume form on  $M$ . One can think of  $\mu_\eta$  as the ‘‘occupancy’’ of the geometry  $\eta$  represents.

**Definition 2** (Normalization). *Let  $\eta \in \Omega^k(M)$  be a  $k$ -form with finite mass. We say  $\xi \in \Omega^k(M)$  is a normalization of  $\eta$  if*

$$\begin{cases} |\xi| \leq 1 & \text{everywhere} \\ |\xi| = 1 & \mu_\eta\text{-almost everywhere} \\ \int_M \omega \wedge \eta = \int_M \star(\omega \wedge \xi) \mu_\eta & \text{for all smooth } (n - k)\text{-forms } \omega. \end{cases} \quad (50)$$

If  $\eta$  is smooth, then  $\xi$  is a normalization of  $\eta$  if  $|\xi| \leq 1$  everywhere, and  $\xi = \eta/|\eta|$  whenever  $|\eta| \neq 0$ .

In the following,  $\delta = (-1)^k \star^{-1} d \star$  denotes the codifferential operator when it is applied to a  $k$ -form.

**Theorem 1** (Optimality of Problem 11). *The optimality condition for the optimizer  $\eta \in \Omega^k(M)$  for Problem 11 is that there exists a normalization  $\xi$  of  $\eta$  such that  $\delta\xi = 0$  (and is subject to the Neumann boundary condition  $j_{\partial M}^* \star \xi = 0$  if  $M$  has boundary,  $j_{\partial M}: \partial M \hookrightarrow M$ ).*

**Theorem 2** (Optimality of Problem 10). *The optimality condition for the optimizer  $\eta \in \Omega^k(M)$  for Problem 10 is that there exists a normalization  $\xi$  of  $\eta$  which is coexact. That is, there exists a form  $\beta \in \Omega^{k+1}(M)$ , called a Kantorovich potential, such that*

$$\zeta = \delta\beta. \quad (51)$$

*If  $M$  has boundary,  $j_{\partial M}: \partial M \hookrightarrow M$ , then the optimality condition also includes a Neumann boundary condition  $j_{\partial M}^* \star \xi = 0$ .*

**Definition 3** (Minimal differential forms). *We call a  $k$ -form  $\eta$  minimal if it admits a coexact normalization. We call a  $k$ -form  $\eta$  cohomologically constrained minimal if it admits a coclosed normalization.*

Note that the normalized (co)closed or (co)exact differential forms are called *calibrated forms* or *calibrations*. We refer readers to *calibrated geometry* [Joyce 2003] if they would like to find out more about calibrated forms.

## A.3 Nonlinear Helmholtz–Hodge Decomposition

Here, we formulate the optimality conditions of Problem 10 and Problem 12 as a Helmholtz–Hodge type decomposition. We first recall the classical Helmholtz–Hodge decomposition.

**A.3.1 Classical Helmholtz–Hodge Decomposition.** For simplicity let us assume  $M$  has no boundary. The classical linear Helmholtz–Hodge decomposition states that each differential form  $\eta_0 \in \Omega^k(M)$  can be uniquely decomposed into

$$\eta_0 = d\alpha + \xi = d\alpha + \delta\beta + \vartheta \quad (52)$$

where  $\alpha \in \Omega^{k-1}(M)$  gives the exact component  $d\alpha$ , and  $\xi$  is coclosed ( $\delta\xi = 0$ );  $\beta \in \Omega^{k+1}(M)$  gives the coexact component  $\delta\beta$ , and  $\vartheta$  is the harmonic form satisfying  $d\vartheta = 0$  and  $\delta\vartheta = 0$ . The pseudo-inverse of  $d^+ \eta_0$  described in Section 2.4 gives the  $(k - 1)$ -form  $\alpha$ . The decomposition (52) can be understood as a summary of the optimality condition for the following least-squares problems. Consider  $\zeta = d\eta_0$  be a given  $(k + 1)$ -form. Then least  $L^2$  norm solution  $\eta$  to  $d\eta = \zeta$ :

$$\underset{\eta \in \Omega^k}{\text{minimize}} \|\eta\|_{L^2} \quad \text{subject to } d\eta = \zeta \quad (53)$$

satisfies the optimality condition given by that  $\eta$  is coexact, *i.e.* there exists  $\beta \in \Omega^{k+1}(M)$  such that  $\eta = \delta\beta$ . Since  $d\eta = d\eta_0 = \zeta$ ,  $\eta_0$  must differ from  $\eta = \delta\beta$  by a closed form. On the other hand, a cohomologically constrained least-squares problem

$$\underset{\eta \in \Omega^k}{\text{minimize}} \|\eta\|_{L^2} \quad \text{subject to } \eta \in \eta_0 + \text{im}(d) \quad (54)$$

has the optimality condition that  $\eta$  is coclosed ( $\delta\eta = \delta(\eta_0 - d\alpha) = 0$ , for some  $\alpha \in \Omega^{k-1}(M)$ ). Hence, in summary, the optimality for (54) gives the *exact-coclosed decomposition*  $\eta_0 = d\alpha + \xi$  where  $\delta\xi = 0$ . The optimization problem (53) gives the *closed-coexact decomposition*  $\eta = (d\alpha + \vartheta) + \delta\beta$ . The uniqueness of the solution to each optimization

problem asserts the uniqueness of the decomposition, leading to  $\xi = \delta\beta + \vartheta$ , and  $\vartheta$  must be closed and coclosed.

**A.3.2 Watertight–Minimal Decomposition.** Using this optimization viewpoint of the classical Helmholtz–Hodge decomposition as models, we state the analogous decomposition related to our minimal mass problems.

Given a  $k$ -form  $\eta_0 \in \Omega^k(M)$ , we evaluate the minimal mass problem for its derivative  $\zeta = d\eta_0 \in \Omega^{k+1}(M)$ . The resulting minimizer  $\eta_1$  is of minimal mass, and the residual  $\eta_0 - \eta_1$  satisfies additional regularity conditions given by the following theorem:

**Theorem 3.** *Each differential form  $\eta_0 \in \Omega^k(M)$  of bounded mass can be decomposed into either*

$$\eta_0 = d\alpha_1 + \eta_1 \quad (55)$$

where  $\eta_1$  is cohomologically constrained minimal and  $d\alpha_1$  is exact, or

$$\eta_0 = (d\alpha_2 + \vartheta) + \eta_2 \quad (56)$$

where  $d\alpha_2 + \vartheta$  is closed,  $\vartheta$  is harmonic, and  $\eta_2$  is minimal. Here,  $\eta_1$  is the minimizer of Problem 12, and  $\eta_2$  of Problem 10 with  $\zeta = d\eta_0$ .

In the special case where  $\eta_0 = \delta_{\Sigma_0}$  is the Dirac- $\delta$  form for some  $(n - k)$ -dimensional submanifold  $\Sigma_0$  in  $M$ , the input  $\zeta = d\eta_0 = d\delta_{\Sigma_0} = (-1)^{k+1}\delta_\Gamma$  is a Dirac- $\delta$  form for the boundary submanifold  $\Gamma = \partial\Sigma_0$ . In that case the optimal solutions  $\eta_1, \eta_2$  in (55) and (56) to the respective minimal mass problem (Problem 10 and Problem 12) are the Dirac- $\delta$  minimal submanifold to the corresponding Plateau problem. In this situation, all  $\eta_0, \eta_1, \eta_2$  are Dirac- $\delta$ , and so are the exact form  $d\alpha_1 = \delta_{\Sigma_1}$  and closed form  $d\alpha_2 + \vartheta = \delta_{\Sigma_2}$ . A surface  $\Sigma$  is called *watertight* if it has no boundary, i.e.  $d\delta_\Sigma = 0$ , or even the boundary of a submanifold  $\delta_\Sigma = d\alpha_1$ . Therefore, we call (55) and (56) decompositions of a given geometry into a watertight and a minimal submanifold.

## B REDUCING PLATEAU PROBLEMS IN $\mathbb{R}^3$ TO $\mathbb{T}^3$

In this appendix, we show that the cohomologically constrained Plateau problem on  $\mathbb{T}^3$  (Problem 4) is equivalent to the Plateau problem in  $\mathbb{R}^3$  with mild additional assumptions.

To be precise, identify  $\mathbb{R}^3$  as the universal cover of  $\mathbb{T}^3$  with a projection  $\pi: \mathbb{R}^3 \rightarrow \mathbb{T}^3$ . Take a closed space curve  $\tilde{\Gamma} \subset \mathbb{R}^3$  and its projection  $\Gamma = \pi(\tilde{\Gamma}) \subset \mathbb{T}^3$  as the boundary data for the Plateau problems in  $\mathbb{R}^3$  and  $\mathbb{T}^3$ . Let  $\mathbf{A} = (A_1, A_2, A_3) \in \mathbb{R}^3$  be the area vector of  $\tilde{\Gamma}$  given by  $\mathbf{A} = \int_{\tilde{\Gamma}} \tilde{\mathbf{y}} \times d\tilde{\mathbf{y}}$  where  $\tilde{\mathbf{y}}: \mathbb{S}^1 \rightarrow \tilde{\Gamma}$  is a parameterization for  $\tilde{\Gamma}$  (cf. (18)). The admissible set of the  $\mathbb{R}^3$ -Plateau problem is given by  $\tilde{\mathcal{A}} := \{\tilde{\eta} \in \Omega^1(\mathbb{R}^3) : d\tilde{\eta} = \delta_{\tilde{\Gamma}}\}$ , whereas the admissible set for Problem 4 is  $\mathcal{A} := \{\eta \in \Omega^1(\mathbb{T}^3) : d\eta = \delta_\Gamma, \int_{\mathbb{T}^3} \eta \wedge \star\partial_i = A_i, i = 1, 2, 3\}$ . Note the additional cohomology constraints  $\int_{\mathbb{T}^3} \eta \wedge \star\partial_i = A_i$  for the problem on  $\mathbb{T}^3$ . Our first goal is to show that there is a correspondence between  $\tilde{\mathcal{A}}$  and  $\mathcal{A}$  related by the projection  $\pi$ : The projection of each object of  $\tilde{\mathcal{A}}$  must lie in  $\mathcal{A}$ , and conversely every object in  $\mathcal{A}$  admits a lift in  $\tilde{\mathcal{A}}$ .<sup>2</sup> Next, we argue that the solution

<sup>2</sup>Showing this correspondence essentially characterizes the lifting property of the geometries in  $\mathbb{T}^3$  to the universal cover  $\mathbb{R}^3$ . What is different from the classical lifting property of covering spaces [Hatcher 2002] is that our geometries are represented by differential forms. Hence, we first establish the projection relationship between the geometries within  $\mathbb{R}^3$  and  $\mathbb{T}^3$  in terms of differential forms in Definition 4.

$\operatorname{argmin}_{\eta \in \mathcal{A}} \|\eta\|_{\text{mass}}$  to Problem 4 is the projection of the solution  $\operatorname{argmin}_{\tilde{\eta} \in \tilde{\mathcal{A}}} \|\tilde{\eta}\|_{\text{mass}}$  of the  $\mathbb{R}^3$ -Plateau problem.

**Definition 4** (Projection  $\pi_\#: \Omega^k(\mathbb{R}^3) \rightarrow \Omega^k(\mathbb{T}^3)$ ). *The projection of a  $k$ -form  $\tilde{\eta} \in \Omega^k(\mathbb{R}^3)$  onto  $\mathbb{T}^3$  is denoted by  $\eta = \pi_\#\tilde{\eta}$  and is defined weakly by that, for all test  $(3 - k)$ -form  $\omega$ ,*

$$\int_{\mathbb{T}^3} \omega \wedge (\pi_\#\tilde{\eta}) := \int_{\mathbb{R}^3} (\pi^*\omega) \wedge \tilde{\eta}. \quad (57)$$

Here,  $\pi^*$  is the pullback operator on differential forms. We say  $\eta$  is the projection of  $\tilde{\eta}$ , and  $\tilde{\eta}$  is a lift of  $\eta$ .

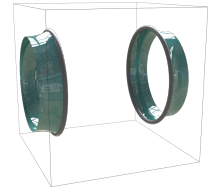
One can check that when  $\tilde{\eta}$  is a Dirac- $\delta$  form, the projection agrees with the projection of the corresponding curves and surfaces. That is,  $\pi_\#\delta_{\tilde{\Sigma}} = \delta_{\pi(\tilde{\Sigma})}$ . One also checks that the projection respects the boundary operator:  $d \circ \pi_\# = \pi_\# \circ d$ . These properties allow one to see that for  $d\tilde{\eta} = \delta_{\tilde{\Gamma}}$ , we have that  $\eta = \pi_\#\tilde{\eta}$  satisfies  $d\eta = \delta_{\pi(\tilde{\Gamma})}$ . Moreover,  $\int_{\mathbb{T}^3} (\pi_\#\tilde{\eta}) \wedge \star\partial_i = \int_{\mathbb{R}^3} \tilde{\eta} \wedge \pi^*(\star\partial_i) = \int_{\mathbb{R}^3} \tilde{\eta} \wedge dx_j \wedge dx_k = A_i$ ,  $\epsilon_{ijk} = 1$ . Hence it is a necessary condition that  $\int_{\mathbb{T}^3} \eta \wedge \star\partial_i = A_i$ . In sum,  $\pi_\#$  maps every element of  $\tilde{\mathcal{A}}$  into  $\mathcal{A}$ .

Conversely, the constraints for  $\tilde{\mathcal{A}}$  are also the sufficient conditions for liftability:

**Lemma 1** (Lifting property). *Given any  $\eta \in \mathcal{A}$ , there exists some  $\tilde{\eta} \in \tilde{\mathcal{A}}$  such that  $\pi_\#\tilde{\eta} = \eta$ .*

**PROOF.** Let  $\tilde{\varphi}: \mathbb{R}^3 \rightarrow \mathbb{R}$  be a compact support function whose translations by the lattice  $\mathbb{Z}^3$  (for the covering of  $\mathbb{T}^3$ ) form a partition of unity  $\sum_{\tau \in \mathbb{Z}^3} \tilde{\varphi}(\mathbf{x} + \tau) = 1$ . In other words,  $\pi_\#\tilde{\varphi} = 1$ . A property that we will use is that  $\pi_\#(\tilde{\varphi}\pi^*\alpha) = \alpha$  for any  $\alpha \in \Omega^k(\mathbb{T}^3)$ .<sup>3</sup> Next, take any  $\tilde{\eta}_0 \in \tilde{\mathcal{A}}$ , and let  $\eta_0 = \pi_\#\tilde{\eta}_0 \in \mathcal{A}$ . Now, let  $\eta$  be an arbitrary element of  $\mathcal{A}$ . Since both  $\eta, \eta_0 \in \mathcal{A}$ , we have  $d(\eta - \eta_0) = 0$  and that  $(\eta - \eta_0)$  is cohomologically trivial  $\int_{\mathbb{T}^3} (\eta - \eta_0) \wedge \star\partial_i = 0, i = 1, 2, 3$ . Therefore,  $\eta - \eta_0$  is exact, i.e. there exists  $q \in \Omega^0(\mathbb{T}^3)$  such that  $\eta = \eta_0 + dq$ . Finally, construct  $\tilde{\eta} := \tilde{\eta}_0 + d(\tilde{\varphi}\pi^*q)$ . Since  $d\tilde{\eta} = \tilde{\eta}_0 = \delta_{\tilde{\Gamma}}$ , we have  $\tilde{\eta} \in \tilde{\mathcal{A}}$ . Moreover,  $\pi_\#\tilde{\eta} = \eta$ , as  $\pi_\#\tilde{\eta} = \pi_\#\tilde{\eta}_0 + \pi_\#d(\tilde{\varphi}\pi^*q) = \eta_0 + d\pi_\#(\tilde{\varphi}\pi^*q) = \eta_0 + dq = \eta$ .  $\square$

What we have shown so far is that  $\mathcal{A}$  is the correct “proxy” of  $\tilde{\mathcal{A}}$  on  $\mathbb{T}^3$ . However, regarding the Plateau problem, there can still be situations where the minimizer  $\bar{\eta} = \operatorname{argmin}_{\eta \in \mathcal{A}} \|\eta\|_{\text{mass}}$  is not the projection of the minimizer  $\tilde{\bar{\eta}} = \operatorname{argmin}_{\tilde{\eta} \in \tilde{\mathcal{A}}} \|\tilde{\eta}\|_{\text{mass}}$  (see inset).



This occurs when  $\bar{\eta}$  represents one of the discrete set of 3-periodic minimal surfaces that (a) connects to the boundary  $\Gamma$  from an adjacent period, (b) still has the same area vector, and (c) has a strictly smaller surface area than the minimal surface represented by  $\tilde{\bar{\eta}}$ . Such a situation is avoided by setting  $\Gamma$  sufficiently distant away from the periodic boundary of the fundamental domain of  $\mathbb{T}^3$ , so as to ensure that the projection of  $\tilde{\bar{\eta}}$  is the global minimizer among the discrete set of 3-periodic minimal surfaces with boundary  $\Gamma$ .

<sup>3</sup>For each test form  $\beta \in \Omega^{3-k}(\mathbb{T}^3)$ ,  $\int_{\mathbb{T}^3} \beta \wedge \pi_\#(\tilde{\varphi}\pi^*\alpha) = \int_{\mathbb{R}^3} \tilde{\varphi}\pi^*\beta \wedge \pi^*\alpha = \int_{\mathbb{R}^3} \tilde{\varphi}\pi^*(\beta \wedge \alpha) = \int_{\mathbb{T}^3} (\pi_\#\tilde{\varphi})\beta \wedge \alpha = \int_{\mathbb{T}^3} \beta \wedge \alpha$ . Hence  $\pi_\#(\tilde{\varphi}\pi^*\alpha) = \alpha$ .